Research Square

Preprints are preliminary reports that have not undergone peer review.
They should not be considered conclusive, used to inform clinical practice,
or referenced by the media as validated information.

An Accessible Recirculating Organ-on-a-Chip Model of Pregnancy-Associated Breast Cancer Reveals ER Stress-Driven Tumour-Placental Cross-Talk

Hagar Labouta

hagar.labouta@utoronto.ca

University of Toronto https://orcid.org/0000-0001-7344-5893

Yasmin Abdelkader
University of Toronto

Mahmoud Abdelkarim
University of Toronto

Paulette Peram
University of Toronto

Matthew Kraljevic
University of Manitoba

Aisha ALSomiry
University of Toronto

Rayan Ramadan
University of Toronto

Laura Edmonds
University of Toronto

Ying Lao
University of Manitoba

Heather Armstrong
University of Alberta

Rene Zahedi
University of Manitoba

Richard LeDuc
University of Manitoba

Article

Keywords:

Posted Date: July 15th, 2026

DOI: https://doi.org/10.21203/rs.3.rs-10018077/v1

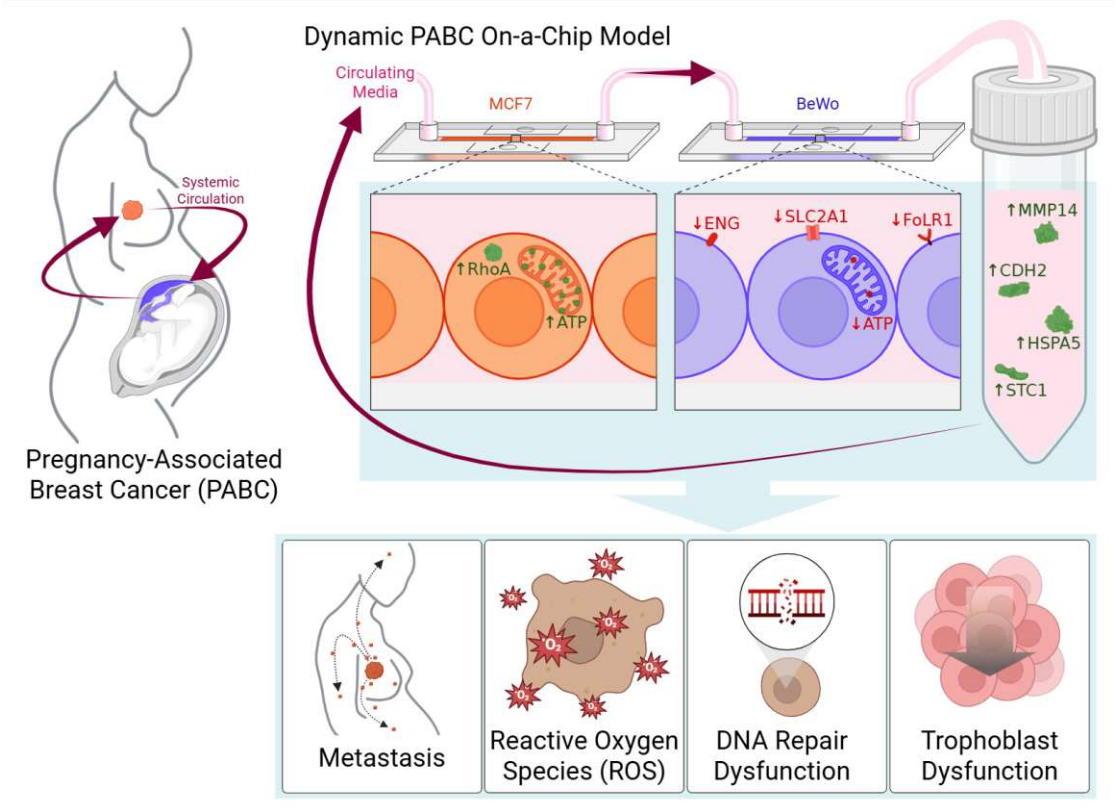
License: This work is licensed under a Creative Commons Attribution 4.0 International License.
Read Full License

Additional Declarations: There is **NO** Competing Interest.

An Accessible Recirculating Organ-on-a-Chip Model of Pregnancy-Associated Breast Cancer Reveals ER Stress-Driven Tumour-Placental Cross-Talk

Yasmin Abdelkader [a,b], Mahmoud Abdelkarim [b,c], Paulette Peram [b], Matthew Kraljevic [d,e], Aisha S. ALSomiry [b], Rayan Ramadan [b], Laura Edmonds [b], Ying Lao [f], Heather Armstrong [d,f,g,h], Rene P. Zahedi [e,f,h,i], Richard LeDuc [d,e], Hagar I. Labouta [a,b,c]

[a] Leslie Dan Faculty of Pharmacy, University of Toronto, Toronto, Ontario, M5S 3M2, Canada
[b] The Keenan Research Centre for Biomedical Science of St. Michael's Hospital, Unity Health Toronto, University of Toronto, Toronto, Ontario, M5B 1T8, Canada,
[c] Institute of Biomedical Engineering, University of Toronto, Toronto, Ontario, M5S 3G9, Canada.
[d] Children's Hospital Research Institute of Manitoba, 513 – 715 McDermot Av. W, Winnipeg, Manitoba R3E 3P4, Canada
[e] Department of Biochemistry and Medical Genetics, University of Manitoba, 745 Bannatyne Av., Winnipeg, Manitoba R3E 0J9, Canada
[f] Manitoba Centre for Proteomics and Systems Biology, 799 JBRC, 715 McDermot Av., Winnipeg, Manitoba R3E 3P4, Canada
[g] Department of Medicine, Division of Gastroenterology, University of Alberta, 11304 – 83 Ave NW, Edmonton, Alberta T6G 2B7, Canada
[h] Department of Internal Medicine, 715 McDermot Av., Winnipeg, Manitoba R3E 3P4, Canada
[i] Cancer Care Manitoba Research Institute, 675 McDermot Av., Manitoba R3E 0V9, Canada



Abstract

Pregnancy-associated breast cancer (PABC) is more aggressive and has a poorer prognosis than non-pregnant breast cancer, yet no preclinical model recapitulates the tumour-placental cross-talk underlying the disease, a major barrier to developing therapies safe for both mother and fetus. We address this with an accessible PABC organ-on-a-chip model built from commercial components. Two single-channel chips seeded with breast cancer and trophoblast cells are coupled into one closed recirculating loop, where a shared medium carries each compartment's secreted factors to the other under physiological shear. This architecture sustains the systemic, bidirectional cross-talk central to PABC that static and single-compartment models cannot, yet needs no microfabrication and runs in any standard laboratory. Using cell-cycle-resolved transcriptomics and secretomics, we found that flow-driven cross-talk activates endoplasmic reticulum stress, marked by HSPA5 upregulation in both cell types, driving tumour invasion, placental dysfunction, and DNA-repair dysregulation. Key molecular signatures aligned with clinical PABC datasets, confirming model relevance. As proof-of-concept, antioxidant coenzyme Q10 reduced trophoblast HSPA5. The model offers a reproducible, accessible system for studying PABC and for screening novel interventions.

Five years after diagnosis, ~89% of women with breast cancer survive, but only ~52% of those diagnosed during pregnancy do [1]. PABC, accounting for nearly 7% of all breast cancers diagnosed per year [2,3], is more aggressive and is often diagnosed at an advanced stage [4], yet how pregnancy reshapes tumour behaviour and how the tumour in turn disrupts placental function remains poorly defined. This gap persists largely because PABC is rare (~1 in 3,000 pregnancies) [2,3], and the ethical constraints of studying pregnant patients make large randomized controlled studies infeasible. As a result, there is no preclinical model of PABC to serve as a screening tool to identify therapeutic targets and evaluate novel interventions for a disease that currently lacks safe options [5,6].

To address this gap, we developed an organ-on-a-chip model of PABC as an early-stage platform for therapeutic screening; no such model currently exists for this disease. The model couples two commercially available microfluidic chips, seeded with breast tumour and trophoblast cells, into a single closed recirculating circuit. Medium circulates unidirectionally, delivering each compartment's secretome to the other over successive cycles; flow is therefore unidirectional while the cross-talk is bidirectional. This circulatory architecture is the central design element, establishing the systemic, continuous tumour-placental communication that static co-culture and single-compartment systems cannot. Requiring no cleanroom, soft lithography, or custom microfabrication, the model reproduces in any standard cell-culture laboratory and can be readily adopted to screen and de-risk candidate therapies at an early stage.

We selected BeWo human placental epithelial cells and MCF7 breast cancer cells to develop our PABC model. BeWo cells are a well-studied model of placental trophoblasts [7-9], and can closely recapitulate key placental features under dynamic flow, such as microvilli formation, syncytialization and hormone secretion, based on our previous work [10]. MCF7 cells were chosen because luminal A subtype, which is positive for estrogen and progesterone receptors, is common in pregnancy and exhibits pregnancy-specific microenvironment changes [11]. These established, widely available lines were chosen to maximize reproducibility and accessibility; as proof-of-concept compartments, they can subsequently be replaced with patient-derived organoids to increase pathological complexity.

To resolve this cross-talk at the molecular level, we used RNA-seq to characterize transcriptomic changes driven by tumor–trophoblast cross-talk, while secretomic (proteomic) analysis of the perfused culture medium identified released proteins that mediate these interactions. Together, these datasets provide comprehensive transcriptomic and secretomic profile of modelled tumour–placental cross-talk in PABC and the regulatory mechanisms driving its inflammatory environment and enables identifying potential downstream targets. Our data shows that endoplasmic reticulum (ER) stress emerged as a central regulator of the tumor–trophoblast cross-talk, coordinating transcriptional and secreted protein changes, summarized in (Fig. 1). ER stress activation

exacerbated disease-related pathways and amplified cancer-associated processes, including oxidative stress, inflammation, epithelial-mesenchymal transition (EMT), and extracellular matrix (ECM) remodeling, all of which are known to drive tumor aggressiveness [12,13]. We then benchmarked the model against clinical PABC datasets and confirmed its responsiveness to therapeutic intervention, establishing a reproducible platform for mechanistic study and early-stage drug screening.

Results

A recirculating two-compartment chip establishes tumour-placental cross-talk in PABC

We constructed the PABC model by coupling MCF7 and BeWo compartments into a single recirculating circuit and benchmarked it against a nested set of controls, static conditioned co-culture, and dynamic single-compartment (MCF7-only, BeWo-only) circuits, so that flow and cross-talk effects could be attributed independently.

To establish a shared perfusion medium compatible with both lines, we screened viability across three basal media under serum-free and serum-containing conditions by Calcein-AM assay at 24, 48, and 72 h (Fig. 2a,b). Both cell types maintained high viability across all media at 24 h, the timepoint used for downstream studies, while certain conditions declined by 48–72 h, most notably F12K serum-free medium for BeWo cells. We selected serum-free DMEM/F12, which sustained viability in both lines and avoided serum-protein interference with downstream secretomics.

Using this optimized medium, we established the dynamic PABC model by culturing MCF7 and BeWo cells on Ibidi$^{0.4}$ microfluidic chips in tandem and perfused under a shear stress of 0.02 dyn/cm², to represent the breast cancer and placental trophoblast compartments, respectively.

The model operated under digitally controlled recirculation: a MUX-driven valve system alternated flow paths to withdraw and reinfuse medium across the 24 h period (Fig. 2c), enabling continuous closed-loop perfusion without manual handling. Each run executed all three circuits (the PABC model and both dynamic controls) in parallel, reducing inter-run variability. Static conditioned controls, with medium exchanged reciprocally between MCF7 and BeWo chips in the absence of flow, provided a no-shear paracrine comparator (Fig. 2d).

Shear stress increases ER stress and ROS production in the PABC model relative to static conditioned culture

Transcriptomic analysis of FACS-sorted cells revealed widespread differential expression in both compartments of the dynamic PABC model relative to static conditioned cultures, at both S and M phases (MCF7: up to ~3,600 upregulated and ~2,800 downregulated

DEGs; BeWo: up to ~2,800 upregulated and ~2,100 downregulated; FDR-corrected; Supplementary Fig. 1a–d). Functional enrichment (GO: BP, CC, MF) of upregulated DEGs in both lines identified endoplasmic reticulum (ER) stress and reactive oxygen species (ROS) metabolic pathways among the top-ranked terms, with Reactome analysis confirming activation of heat-shock and general stress-response pathways (Fig. 3a).

Among ER stress–related genes, HSPA5 and HSP90B1 were significantly upregulated in MCF7, and HSP90AA1 and HSP90AB1 in BeWo, at S phase versus static controls (Fig. 3b,c). Consistent with these signatures, secretomic analysis showed increased HSPA5 protein in the dynamic PABC media (fold change = 2.05; Supplementary Fig. 2), and western blot confirmed elevated HSPA5 in both BeWo and MCF7 lysates (Fig. 3d–i). BeWo cells showed a higher relative fold change than both their dynamic and static controls, whereas MCF7 levels were comparable to controls (Fig. 3d–i).

ER chaperones are the central mediators of ER stress-driven tumour-placental cross-talk in the PABC model

To identify mediators of the ER stress–driven cross-talk, we constructed protein-protein interaction (PPI) networks from the differentially expressed proteins (DEPs) circulating in the dynamic PABC model versus static cultures, enriched with first-interactor non-DEPs to reveal central hub proteins. Among upregulated proteins, the ER chaperone calnexin (CANX) emerged as the top-ranked hub (k = 256), suggesting a central role in coordinating ER stress responses (Fig. 3j). Among downregulated proteins, CAPZB was the most connected (k = 455), implicating cytoskeletal organization and trafficking alterations previously linked to breast cancer development [14,15] (Fig. 3k). The full ranked DEP and non-DEP networks are provided in Supplementary Tables 1-4.

Adaptive mechanisms to mitigate ER stress and ROS are induced in the PABC model

Alongside ER stress, GO and Reactome analyses revealed coordinated activation of adaptive stress-response programs in both compartments of the dynamic PABC model: the unfolded protein response (UPR), the ubiquitin–proteasome system (UPS) including ER-associated degradation (ERAD), autophagy and mitophagy, and antioxidant defenses through the KEAP1–NFE2L2 pathway (Fig. 3l–s). Key effectors were upregulated across these programs, including the chaperones HSPA5 and ATF4/ATF6, autophagy genes (ATG3, ATG5, MAP1LC3B), and antioxidant genes (HMOX1, NQO1, SOD1), indicating that cells engage compensatory mechanisms to counter the sustained ER and oxidative stress.

ER stress induces coordinated mitochondrial activation, biogenesis, and metabolic rewiring in MCF7 cells of the PABC model

Mitochondrial activity was enhanced in MCF7 cells of the dynamic PABC model relative to static conditioned cultures, with enrichment of oxidative phosphorylation, ribosomal assembly, NADH activity, and mitochondrial biogenesis (Fig. 4a). The calcium-transport pathway was activated, with significant upregulation of the outer-membrane channel VDAC1 and the mitochondrial Ca^{2+} uniporter MCU (Fig. 4b), indicating enhanced ER-mitochondrial coupling [16,17]. Consistent with this, pyruvate and fatty-acid metabolism converged on acetyl-CoA, supported by upregulation of the glucose transporter GLUT3 and the fatty-acid transporter SLC27A3 at S phase (Fig. 4c,d). Acetyl-CoA in turn fed the mevalonate pathway, with an upward trend in its rate-limiting enzymes HMGCR and MVK (increased mean expression, not statistically significant; Supplementary Fig. 3), while secretomic analysis showed elevated prenylated proteins (NRAS, HRAS, RAC) that activate downstream PI3K and MAPK signaling (Fig. 4e,f). Together, these pathways link mitochondrial activation to acetyl-CoA–driven metabolic rewiring and oncogenic signaling (Fig. 4g).

ER stress disrupts DNA repair, and promotes cell-cycle progression and mitotic activity in MCF7 cells of the PABC model

GO and Reactome enrichment revealed activation of DNA-repair pathways responding to double-strand breaks, including the ATR and homologous recombination (HRR) pathways (Supplementary Table 5), with detection of CHEK1, BRCA2, and RAD51. Notably, BRCA1 was significantly downregulated in MCF7 of the dynamic PABC model versus static culture at S phase (Fig. 5a). In parallel, p53 signaling was activated alongside significant upregulation of the cyclin inhibitor CDKN1A and the mitotic kinase CDK1 at S phase (Fig. 5b), and GO enrichment confirmed activation of DNA-replication and cell-division pathways (Supplementary Table 6). The APC/C complex was also activated at M phase, with significant upregulation of CDC20, which drives the metaphase-to-anaphase transition during mitosis, and CCNB1, a regulator of mitotic entry (Fig. 5c), both higher in M than S phase (Fig. 5d). The mitotic checkpoint complex (BUB3, BUB1B, MAD2L1), required for accurate chromosome segregation in M phase, was activated at both phases with comparable expression (Fig. 5d). Together, these findings indicate accelerated mitotic progression despite impaired checkpoint control, consistent with BRCA1 loss (Supplementary Table 5).

RhoA/ROCK2 signaling drives EMT, ECM remodeling, and inflammation in tumour cells of the PABC model

To test whether tumour–placental cross-talk promotes cancer-associated phenotypes, we examined genes related to angiogenesis, EMT, and ECM remodeling by GSEA (Supplementary Table 7). Of the genes shared across inflammation, EMT, and angiogenesis, Circos analysis highlighted enrichment of Rho-family signaling, cell migration, stress-fiber assembly, and cytokinesis pathways (Fig. 6a,b). RhoA and ROCK2

were consistently enriched across these pathways, with RhoA significantly upregulated in the dynamic PABC model versus static culture at M phase (Fig. 6c). Consistent with an EMT shift, integrins ITGA3 and ITGB4 were downregulated (Fig. 6d), and the secretome showed increased mesenchymal markers N-cadherin (CDH2) and vimentin with a corresponding decrease in E-cadherin (CDH1) (Fig. 6e); western blot confirmed elevated N-cadherin in MCF7 lysate relative to static and dynamic controls (Fig. 6f-h). Inflammatory TGFβ1 signaling (TGFβ1, TGFβR1) was activated (Fig. 6j), although ELISA showed the highest latent TGFβ1 in the static culture rather than the dynamic models (Fig. 6i).

Tumour-placental cross-talk under dynamic conditions promotes a pro-remodeling extracellular matrix milieu

To determine how the intracellular RhoA/ROCK2-driven changes extend to the extracellular environment, we performed hierarchical clustering of the proteins secreted across dynamic and static conditions, which resolved into nine expression clusters (Fig. 7a; Supplementary Table 8). Proteins upregulated in the dynamic PABC media versus static cultures were enriched in ECM remodeling and adherens-junction organization, alongside mechanical-stress and inflammatory pathways (Fig. 7b). ECM remodeling was driven by matrix metallopeptidase MMP14 and a tightly interconnected collagen network (COL1A1, COL1A2, COL2A1, COL3A1, COL4A3, COL6A1, COL11A1), which STRING analysis showed recurred consistently across these pathways (Fig.7c). Together, these changes indicate a pro-remodeling extracellular environment that could facilitate cancer metastasis.

ER stress drives ATR-linked cell-cycle dysregulation and suppresses angiogenesis, nutrient transport, and adhesion in trophoblasts of the PABC model

We next examined whether tumour-placental cross-talk alters placental function in BeWo cells versus static culture. BeWo cells exhibited pronounced ER stress with activation of DNA-repair pathways across both S and M phases, including TP53 and ATR responses to replication stress and double-strand breaks (Fig. 8a,c). DNA-replication pathways remained active during M phase while mitotic pathways persisted in S phase (Fig. 8b,c), indicating disrupted phase-specific cell-cycle transitions. Using the GSEA database, we identified significant downregulation of key angiogenic markers (FGFR1, FGFR2, ENG, EGFR; Fig. 8d) and MMP14 (Fig. 8e); glucose and fatty-acid transporters (SLC2A1, SLC2A3, SLC27A1; Fig. 8f); mineral and iron transporters (KCNH5, KCNJ6, SLC41A1, SLC25A37; Fig. 8g) and the folate transporter FOLR1 (Fig. 8h); adherens-junction genes of the ITGA family (Fig. 8i); and the cell-cycle kinases PAK1 and PIK3C2G (Fig. 8j).

Placental-tumour cells cross-talk in the PABC model drive enhanced oncogenic signaling distinct from non-pregnant breast cancer modeled by the dynamic MCF7 control model

To isolate how placental cues specifically shape the breast cancer phenotype during pregnancy, we compared MCF7 cells in the dynamic PABC model against a non-pregnant dynamic MCF7 control. At S phase, 3 genes were upregulated and 5 downregulated (Supplementary Fig. 4): the upregulated genes drove oncogenic signaling (NR4A1, STIL), while the downregulated ferritin pseudogenes FTH1P2 and FTLP3, which regulate FTH1 and oxidative-stress control [18,19], suggested altered redox balance. At the secretome level, 132 upregulated proteins were enriched in cell-junction, TGFβ signaling, ECM, and angiogenesis pathways (Fig. 9a), with overlapping mediators including NOTCH1, ENG, FGFR2, PGF, and ADAM9. PPI network analysis identified HLA-B (k = 144) and amyloid precursor protein APP (k = 95) as the top hubs (Fig. 9b; Supplementary Table 9), indicating co-activation of immune response and oncogenic signaling.

Together, these findings show that placental-derived soluble factors are sufficient to reprogram oncogenic, ECM, and angiogenic signaling in breast cancer cells, establishing a phenotype distinct from non-pregnant breast cancer under identical flow.

Tumour-derived cues disrupt trophoblast cell-cycle, cytoskeleton, adhesion, and transport relative to the dynamic BeWo control

Conversely, to isolate the effect of tumour-derived signals on placental function, we compared BeWo cells in the dynamic PABC model against a tumour-free dynamic BeWo control. Transcriptomic profiling identified 10 upregulated and 430 downregulated genes at S phase (Supplementary Fig. 5). The upregulated genes (H2BC9, BPTF, CHD4) were linked to chromatin remodeling and DNA repair, while downregulated genes were enriched in actin cytoskeleton, focal adhesion, and ECM pathways (Fig. 10a), with significant loss of structural genes FSCN1, PKP3, and BCAM (Fig. 10b), indicating impaired cytoskeletal integrity. Cell migration and embryo-implantation pathways were also reduced (Fig. 10a), and cytotrophoblast proliferation markers (RRM2, CCNB1, CDK1) declined (Fig. 10c), alongside downregulation of cell-cycle and growth signaling (RAC1, CDC42, AMPK pathways; regulators AKT2, CCND3, CSNK1D, MAPK7) (Fig. 10d,e). Placental transport was likewise disrupted, with reduced expression of the glucose transporter SLC2A8 (GLUT8), folate transporters SLC19A1 and SLC46A1, amino-acid transporters SLC1A5 and SLC7A5, and the iron transporter ABCC10 (Fig. 10f,g). Angiogenic signaling was impaired, with significant reductions in GATA2 and HGS (Fig. 10h,i).

Functional validation of cytoskeletal and junctional disruption in BeWo cells of the PABC model

To validate the transcriptomic evidence of impaired actin cytoskeleton organization and cell–cell junction integrity, we performed confocal imaging and quantitative morphometric analyses of filamentous and cortical actin, as well as ZO-1 tight junctions, in BeWo cells of the dynamic PABC model, control dynamic BeWo model and static conditioned BeWo cultures (Fig. 11a).

Morphometric analysis demonstrated that dynamic conditions enhanced the circularity of the nuclei of BeWo cells compared to those in the static conditioned culture. The highest nuclear circularity was observed in the control dynamic BeWo model (0.50), compared with the dynamic PABC model (0.42; $p = 0.03$) and the static conditioned culture (0.35; $p = 0.06$) (Fig. 11b), while no significant differences in nuclear size were observed across conditions. These findings suggest that tumour-derived cues partially reverse the structural benefits conferred by physiological flow. Consistent with transcriptomic evidence of junctional disruption, ZO-1 pocket size increased in the BeWo cells of the dynamic PABC model, accompanied by disorganization of tight junction architecture compared to both control dynamic BeWo model and static conditioned BeWo cultures (Fig. 11c). Actin pocket sizes were comparable between the dynamic PABC model and static conditioned BeWo culture and elevated relative to the control dynamic BeWo model, though differences were not statistically significant (Fig. 11d).

Quantitative actin fibral analysis using FibrilTool confirmed the downregulation of actin cytoskeleton filaments in BeWo cells of the dynamic PABC model. Analysis of fibril anisotropy demonstrated lesser assembly of actin fibrils in the dynamic PABC model compared with the control dynamic BeWo model and static conditioned BeWo cultures. Fibril anisotropy analysis revealed the lowest actin filament assembly in the dynamic PABC model (0.13), compared to the control dynamic BeWo model (0.17) and the static conditioned BeWo cultures (0.21). The difference between static conditioned culture and dynamic PABC conditions was statistically significant ($p = 0.048$), indicating disrupted actin stress fiber organization in response to tumour-placental cross-talk (Fig. 11e). No significant differences were observed in stress fiber angle variance across models. These results further confirm placental dysfunction in conditions of pregnancy-associated breast cancer due to impairment of trophoblast cytoskeletal organization and tight junction integrity.

Circulating stress-inducible factors, heat-shock proteins and metabolic regulators mediate tumour-driven disruption of placental function in the PABC model

To identify the circulating factors driving these placental changes, we profiled the secretome of the dynamic PABC model versus the dynamic BeWo control. Among 29 proteins with elevated secretion, GO enrichment highlighted fructose metabolism, vitamin-D response, calcium import, and cAMP pathways (Supplementary Fig. 6a). Stanniocalcin-1 (STC1), a stress-inducible cytoprotective factor, recurred across these

pathways and was significantly elevated in the dynamic PABC model (Supplementary Fig. 6b), pointing to a central role in tumour-induced placental stress. Consistent with a stress-adaptive secretory profile, KEGG and Reactome analyses showed enrichment of the pentose phosphate pathway, fructose and mannose metabolism, and gluconeogenesis, driven by elevated FBP1 and FBP2 (Supplementary Fig. 6b,c). PPI network analysis identified the heat-shock protein HSPB1 (k = 82) and EPHA7 (k = 57) as the top hubs (Supplementary Fig. 6d; Supplementary Table 10), underscoring activation of heat-shock and stress-response signaling. These findings indicate that tumour-placental cross-talk in the dynamic PABC model generates a stress-adaptive secretory milieu enriched in stress factors, heat-shock proteins and metabolic regulators, providing a mechanistic basis for the transcriptomic suppression of cell-cycle activity, cytoskeletal organization, adhesion, and nutrient transport observed in BeWo cells of the dynamic PABC model.

Clinical benchmarking confirms the model reproduces Key molecular signatures in both compartments

To establish that the model's outputs reflect human disease rather than cell line-specific artefacts, we benchmarked the PABC model against patient data in three tiers: the tumour and trophoblast compartments were each validated independently under flow, against breast cancer transcriptomes and primary placental data, respectively, before the coupled model was validated against clinical PABC signatures. Validating each compartment before coupling isolates the contribution of cross-talk from the behaviour of either cell type alone.

We first evaluated whether MCF7 cells cultured under tumour-only dynamic conditions recapitulate transcriptional programs observed in human breast cancer. Transcriptomic profiles from the control dynamic MCF7 model were compared with gene expression data from The Cancer Genome Atlas (TCGA) database invasive ductal carcinoma patients (BRCA1 project; *n* = 1097 patients). We observed similar expression patterns of key oncogenic and breast cancer invasiveness-associated genes (Fig. 12a-i). These findings validate the control dynamic MCF7 model as an appropriate pathological baseline for comparison with the dynamic PABC model.

Next, we assessed whether BeWo trophoblasts cultured under placental-only dynamic conditions retain transcriptional features consistent with human placental biology. Gene expression profiles from the control dynamic BeWo model were compared with publicly available gene expression data from human placental tissues which were retrieved from the GEO database with accession number GSE89497, encompassing gene expression profiles of different placental cell types at various gestational stages at 8- and 24-week gestation [20]. We compared key identified genes at both S and M phase of BeWo cell line under dynamic conditions with gene expression pattern of cytotrophoblast layer (CTB). CSH1 expression was not statistically different in either the S or M phases relative to

cytotrophoblast expression levels. In contrast, the expression patterns of ENG, HGS and SLC38A10 were more consistent with the M-phase profile than S phase profile (Fig. 12j-r). This alignment shows the potential relevance of the dynamic BeWo control as a model of placental trophoblast function under flow.

Having validated each of the control dynamic models, we next examined whether the dynamic PABC model captures transcriptional features unique to PABC. We compared transcriptomic signatures from MCF7 cells in our PABC model with publicly available clinical PABC datasets obtained from the Gene Expression Omnibus (GEO) (accession number GSE31192), which include invasive ductal carcinoma (Stage III) with positive tumor for estrogen receptor (ER), progesterone receptor (PR), and BRCA1 mutations [13]. MCF7 cells within our dynamic PABC model displayed expression levels of key identified genes that closely mirrored those observed in clinical PABC samples, with stronger similarity during S phase than M phase (Fig. 12s-mm). Together, these tiers confirm that the model reproduces PABC molecular signatures in both compartments and in their coupling establishing that the cross-talk it captures is disease-relevant, not a cell-line artefact. This supports the model's use for mechanistic study and early therapeutic screening in a disease where patient material is scarce and direct experimentation constrained.

Coenzyme Q10 treatment demonstrates the model's responsiveness to therapeutic intervention

Beyond reproducing PABC biology, a screening platform must register a measurable response when a candidate intervention is applied. As proof-of-concept, we treated the PABC model with coenzyme Q10 (CoQ10, 10 μM), an antioxidant that modulates oxidative stress and mitochondrial function, and used HSPA5, the model's central stress marker, as the readout. CoQ10 reduced relative fold change of HSPA5 protein levels in BeWo cells relative to untreated PABC model (Fig. 13a), while MCF7 levels were unchanged (Fig. 13b), indicating a compartment-specific response detectable at the protein level. This establishes that the platform reports therapeutic modulation of a disease-relevant target, the functional capability required to screen and prioritize candidate interventions.

Discussion

PABC is a clinically distinct disease in which tumour progression unfolds within the unique environment of pregnancy, yet the cross-talk between tumour and placenta that shapes its behaviour has remained poorly defined for lack of physiologically relevant models. Our dynamic PABC platform integrates breast cancer and trophoblast cells under shear and shared circulation, revealing emergent tumour and placental phenotypes absent from static or dynamic single-compartment models.

A key finding of this work is that tumour-placental cross-talk under flow established a coordinated stress-adaptation response dominated by ER stress, acting as an upstream driver of both cancer aggressiveness and placental dysfunction. Sustained elevation of GRP78/HSPA5 across the transcriptome and secretome of both cell types (Fig. 3b, d-i) indicates a persistent rather than transient response. GRP78/HSPA5 is a well-established driver of breast cancer metastasis, drug resistance, and poor outcome through its interaction with the estrogen receptor and enhancement of tamoxifen resistance [21-23,24-26]; its persistence here suggests that the pregnant microenvironment, coupled to tumour cues under flow, reinforces stress-adaptive pathways favouring tumour progression.

In tumour cells, this ER stress drove mitochondrial reprogramming and metabolic rewiring. Elevated mitochondrial biogenesis and calcium influx (VDAC1, MCU; Fig. 4a) are consistent with GRP78/HSPA5-mediated ER–mitochondrial Ca^{2+} transfer [27-29], and the resulting ROS and lipid metabolism fed acetyl-CoA–dependent pathways including the mevalonate pathway (HMGCR, MVK), both linked to poor breast cancer outcome[30,31]. The accompanying rise in prenylated proteins (NRAS, HRAS, RAC) activating PI3K and MAPK signaling (Fig. 4e,f), pathways repeatedly reported in PABC patients [32-34], links this metabolic shift to oncogenic signaling and a mechanistic basis for the aggressive tumour phenotype. In parallel, cross-talk activated RhoA/ROCK signaling specifically at M phase; given RhoA's role in cytokinesis[43], this explains the enrichment of cytokinesis and spindle-assembly pathways (RhoA, ROCK2; Fig. 6b,c). Beyond division, shear-driven RhoA activation promotes the cytoskeletal reorganization underlying EMT, migration, and angiogenesis [35,36], consistent with the enrichment of these pathways and the secreted collagen complexes we observed (Fig. 7). A latent inflammatory response accompanied this shift: TGFβ signaling remained upregulated (Fig. 9ii) despite reduced latent TGFβ in lysate, likely reflecting its proteasomal degradation under flow [37], and was reinforced by NR4A1, a TGFβ/SMAD activator promoting EMT[38]. The cadherin switch (CDH1 loss, CDH2 gain; Fig. 6e-h) confirmed acquisition of a mesenchymal, invasive phenotype.

On the placental side, the same ER stress translated into broad functional suppression. Angiogenesis (GATA2, GATA3, PGF; Fig. 10i) and transport of glucose, folate, amino acids, and iron (Fig. 10g), all essential for fetal development, were downregulated, recapitulating placental insufficiency [39-42]. MMP14 transcript, critical for trophoblast invasion [43], was suppressed in trophoblasts (Fig. 8e), yet MMP14 protein was elevated in the circulating medium, likely tumour-derived, consistent with the ECM remodeling reported in PABC [44]. Cytoskeletal regulation was likewise disrupted, with downregulation of trophoblast Rho/Rac/Cdc42 GTPases [45,46] (Fig. 10d) and the organization genes FSCN1, FLNA, VASP, DAG1, and ZYX, whose loss is linked to recurrent miscarriage [47-49]. Confocal imaging confirmed disorganized actin and enlarged ZO-1 pockets reflecting compromised tight junction integrity (Fig. 11a), and STC1, a cytoprotective hormone elevated in stressed placentas [50,51], was secreted only in the PABC model, indicating a

compensatory but insufficient response. Together these changes recapitulate placental stress disorders and offer a mechanistic explanation for adverse pregnancy outcomes observed in PABC, including preterm birth and fetal growth restriction [52-54].

Phase-resolved analysis of S and M populations revealed that prolonged ER stress induced DNA damage in both compartments, with divergent responses not visible in bulk analysis. In MCF7 cells within the PABC model, ATR–CHEK1 checkpoint signaling was activated, with p53-mediated induction of the cell-cycle inhibitor CDKN1A, a signal that should arrest the cycle for repair [55,56]. Yet, in parallel, CDK1 and DNA-replication pathways were upregulated (Fig. 5b; Supplementary Table 6), and the cells continued to divide. This co-occurrence, an engaged checkpoint alongside sustained proliferation, indicates that MCF7 cells override the arrest signal and progress through the cycle despite unrepaired DNA damage. By contrast, BeWo cells showed ATR-associated arrest between S and M phases. Impaired homologous recombination repair, reflected by enrichment of BRCA1 loss-of-function pathways (Supplementary Table 5), suggests compromised DNA repair and increased genomic instability [57-60], and is consistent with previous studies linking BRCA1 increased susceptibility to PABC [61,62]. While elevated Cdc20, CCNB1, and checkpoint regulators (BUB1B, BUB3, MAD2L1) indicate premature APC/C activation and mitotic slippage [63-65]. These findings agree with the GEICAM-EMBARCAM study, which reported enriched DNA-repair pathways and Cdc20 activation in PABC tumours [12], and together suggest that concurrent BRCA1 loss and early APC/C activation drive mitotic progression with unresolved DNA damage.

Clinical benchmarking confirmed that both compartments capture transcriptional programs reported in patient-derived breast cancer and placental datasets, and the model responded functionally to antioxidant intervention, with CoQ10 reducing trophoblast HSPA5 (Fig. 13a) in line with its reported protection against placental oxidative stress [66,67]. Together these establish that the model reflects disease-relevant PABC biology and reports therapeutic modulation of a disease-relevant target, supporting its use to screen and de-risk candidate interventions.

The model reflects deliberate trade-offs favouring reproducibility and accessibility, but several design choices warrant consideration. Though choriocarcinoma-derived, BeWo is a validated trophoblast model reproducing syncytialization and hormone secretion under flow, and retaining cytotrophoblast transcriptional features under flow in our benchmarking (Fig. 12). A single tumour line cannot capture full PABC heterogeneity, but the modular architecture accepts patient-derived organoids, immune cells, and hormonal inputs without redesign, and supports higher or compartment-specific shear as needed. Each defines a route for extension while preserving a reproducible, accessible system that faithfully reports PABC biology.

Conclusion

We present an accessible, recirculating organ-on-a-chip model that reconstitutes tumour–placental cross-talk in PABC using only commercial components. The model identified prolonged ER stress, mediated by GRP78/HSPA5, as a central driver of coordinated tumour and placental dysfunction, promoting an invasive, RhoA–ROCK-driven phenotype in tumour cells and suppressing nutrient transport and angiogenesis in trophoblasts, and its molecular signatures aligned with clinical PABC datasets. These findings nominate GRP78 and RhoA–ROCK as druggable targets and, more broadly, establish a reproducible platform that any laboratory can adopt to study PABC and to screen and de-risk candidate therapies before animal testing.

Methods

Cell culture & optimization of cell culture conditions

The human breast adenocarcinoma cell line MCF-7 (ATCC® HTB-22™, USA) and the human placental choriocarcinoma BeWo b30 subclone (provided by Dr. Tina Bürki, EMPA, Switzerland, with permission from Prof. A. Schwartz, Washington University in St. Louis, USA) were used to model breast cancer and placental trophoblasts, respectively. Cells were maintained at 37°C in a humidified incubator with 5% CO_2. To identify a suitable shared culture media for the dynamic PABC model, three basal media were evaluated: Ham's F-12K (Kaighn's modification of Ham's F-12) medium (Gibco™, Thermo Fisher Scientific, cat. no. 21127022, USA), DMEM/F-12 (1:1 mixture of Dulbecco's Modified Eagle's Medium and Ham's F-12; Gibco™, Thermo Fisher Scientific, cat. no. 11320-033, USA), and high-glucose DMEM (4.5 g L^{-1} glucose; Sigma-Aldrich, cat. no. D5796). Each basal medium was tested either with 10% (v/v) fetal bovine serum (FBS; Corning®, cat. no. 35-077-CV, Canada) or under serum-free conditions (SFM). Both SFM and FBS-supplemented media included 1% (v/v) penicillin–streptomycin antibiotic mixture (Corning®, cat. no. 30-002-CI, USA) to prevent microbial contamination. We selected serum-free media to avoid FBS interference with downstream secretomic analyses.

Cell viability screening

Cells were seeded in black-walled, clear-bottom 96-well plates (Corning®, cat. no CLS3603, USA) at a density of 250,000 cells per well in 100 µL of the respective medium. We assessed viability at 24, 48, and 72 hours using a Calcein-AM assay (Invitrogen™, Thermo Fisher Scientific, cat. no. C3100MP, USA) according to the manufacturer's instructions. Briefly, cells were washed once with phosphate-buffered saline (PBS; Gibco™, Thermo Fisher Scientific, cat. no. 10010023, USA) and incubated with Calcein-

AM working solution at a final concentration of 2 μM in SFM for 30 minutes at 37 °C in the dark. Fluorescence was measured using a Synergy™ H1 Hybrid Microplate Reader (Agilent BioTek Instruments, USA) at excitation/emission wavelengths of 490/520 nm. We chose the 24 hour time point for further experiments because both cell types showed high viability across all tested media at this time, while avoiding the variability and decline observed at later time points (Fig. 1a, b). We selected DMEM/F-12 SFM as the common perfusate for the PABC model.

Dynamic & static models

MCF7 and BeWo cells were cultured into microfluidic chips (μ-Slide I $^{0.4}$ Luer flow chambers (ibidi, Germany), with a channel length of 50 mm, width of 5.0 mm, and a growth area of 2.5 cm². Cells were maintained in DMEM/F12 medium supplemented with 10% FBS and 1% penicillin until reaching 60–70% confluency. Before initiating the dynamic experiments, cells were washed three times with PBS and three times with SFM. SFM was then added to the cells, and the chips were connected in series within a single closed-loop flow circuit (Fig. 1c), with the MCF7 and BeWo chips sharing one continuously recirculating medium. Each circuit included a three-way valve and a syringe pump to recirculate the medium. A multi-channel syringe pump (DK InfuseTek, model ZU-I) was used to withdraw and infuse the culture medium at 16 μL/min, creating an estimated wall shear stress of 0.02 dyn/cm² in the chip channels. Estimated wall shear stress $\tau = (6\mu Q)/(wh^2)$, assuming $\mu = 1$ mPa·s at 37 °C, ≈0.02 dyn/cm² for an Ibidi μ-Slide I$^{0.4}$ channel ($h = 400$ μm, $w = 5$ mm). Flow was applied for 24 hours to simulate the physiological conditions of cells[68,69]. Dynamic control experiments were run in parallel under identical flow and shear conditions using MCF7-only or BeWo-only chips.

For static conditioned controls, MCF7 and BeWo cells were cultured in microfluidic chips at the same density, with each biological replicate pooled from 3 chips, and maintained in cell culture medium followed by washing as described for the dynamic experiments before incubation in SFM for 24 hours. After 24 hours, the conditioned media from each cell type was collected, centrifuged at 17,000 xg for 10 minutes to remove cell debris and the supernatants were swapped (MCF7 conditioned medium added to BeWo static cultures, and vice versa). These static conditioned cultures were incubated for additional 24 hours, matching the dynamic experiment duration. This static conditioned medium setup served as a control for paracrine exchange in the absence of shear flow.

Fluorescence-Activated Cell Sorting (FACS) and RNA sequencing

After 24 hours of dynamic experiments and static controls, cells were collected from the chips for FACS using a BD FACSAria™ III cell sorter (BD Biosciences, USA). MCF7 and BeWo cells from the dynamic PABC model, control dynamic, and static models were sorted into S-phase and M-phase populations. Cells were detached using 0.25%Trypsin-

EDTA (0.25% trypsin with EDTA 4Na; Gibco™, Thermo Fisher Scientific, cat. no. 25200-072, Canada) and neutralized with Trypsin Neutralizer Solution (TNS; Gibco™, Thermo Fisher Scientific, cat. no. R-002-100, USA). Cells were stained for DNA content using Vybrant™ DyeCycle™ Green stain (Thermo Fisher Scientific, cat. no. V35004, USA), and S-phase and M-phase cell populations were isolated using a standard DNA content gating method which is based on defining forward and side scatter parameters to exclude debris and doublets. Sorted cells were immediately processed for RNA extraction with RNeasy Micro kit (QIAGEN, cat. no. 74004, Germany). We quantified the RNA and checked its quality using Agilent NGS Bioanalyzer RNA quality control system (Agilent Technologies, USA), and only samples with RNA integrity number (RIN) greater than 7 were used for downstream analysis. Then, RNA libraries were prepared using the NEBNext® Single-Cell/Low Input RNA Library Prep Kit (New England Biolabs). Library preparation and sequencing were performed at hospital for sick children (SickKids) Toronto, Ontario. Prepared libraries were sequenced on an Illumina NovaSeq™ X using a 10B flow cell with a 300-cycle configuration, generating paired-end reads of 150 bp with sequencing depth 30-50 million paired end reads.

Transcriptomics

A total of 72 total bulk RNA-Sequencing (RNA-seq) datasets were generated from the PABC model, dynamic controls and static conditioned cultures during the S and M phases. In total, 2.7 billion reads were obtained, comprising 1.25 billion unique reads and 1.45 billion duplicate reads, with an average of 17,304,058.9 unique reads and 20,148,747.46 duplicate reads per file. The overall average read length was 250. Data processing was performed in accordance with established transcriptomic analysis protocols implemented in the Galaxy platform from Betut et al [70,71]. Analyses were conducted using the Galaxy web platform and RStudio server hosted on the high-performance computing infrastructure of the Children's Hospital Research Institute of Manitoba. FASTAQ sequences were quality-checked using FastQC (http://www.bioinformatics.babraham.ac.uk/projects/fastqc) (Galaxy Version 0.73+galaxy0), and results were aggregated using MultiQC[72] (Galaxy Version 1.11+galaxy0). Adapter sequences, reads shorter than 20 bp and reads with an average Phred score below 20 were removed using Cutadapt [73] (Galaxy Version 4.0+galaxy0). Filtered reads were aligned to the human reference genome (Ensembl version Homo_sapiens.GRCh38.111) using STAR [74]aligner. Gene expression quantification and normalization were performed using DESEQ2 [75] in R. Differential expression analysis was conducted on normalized count data using a linear modeling approach implemented in R (https://www.rdocumentation.org/packages/stats/versions/3.6.2/topics/lm). DESEQ2 comparisons were conducted as follows: MCF7 and BeWo cells within the dynamic PABC model at both S and M phases were compared against corresponding cell types and

phases in static conditioned cultures and dynamic control models with FDR-corrected (5%).

Secretomics

Secretomic analysis was conducted to quantify proteins secreted into the culture media across dynamic and static conditions. Approximately 10µg of protein per sample were precipitated using 20% tricholoracetic acid (TCA) overnight, followed by centrifugation at 17,000 xg for 30 min at 4˚C. Protein pellets were washed twice with 250 µL of cold acetone, and dried in a speedvac concentrator. Next, protein pellets were re-dissolved in 50 µL of 4% SDS, 100 mM HEPES, pH 8.0. Disulfide bonds were reduced with 10 mM DTT at 57˚C for 30 minutes, and free cysteines were alkylated with 50 mM iodoacetamide at RT for 45 minutes in the dark. Protein samples were digested using Strap micro columns (Protifi) according to the manufacturer's protocol and using Trypsin/LysC (Promega) at a 1:10 enzyme to protein ratio, for 2 hours at 47˚C. Digested samples (200 ng) were loaded on Evotips and analyzed using a DIA-PASEF on a TimsTOF Pro2 (Bruker) coupled to an EvosepOne.

Raw data were processed using DIA-NN 1.8.2 beta [76]. An in-silico spectral library was generated using the human Swissprot proteome (downloaded July 24, 2023; 20,399 target sequences). Data was filtered at 1% false discovery rate, leading to 4998 reported proteins. Only proteins that were quantified with at least 2 peptides with a quality value >0.75 in at least 2 out of 3 replicates of at least 1 condition were kept for data analysis. After this filtering, a total of 3795 high quality proteins were kept for statistical analysis, and all protein intensities were log2-transformed. The following individual proteome comparisons were performed: (i) circulating media from the dynamic PABC model vs circulating media from the control dynamic MCF7 model, (ii) circulating media from the dynamic PABC model vs circulating media from the control dynamic BeWo model, (iii) circulating media from the dynamic PABC model vs static conditioned MCF7 culture media, and (iv) circulating media from the dynamic PABC model vs static conditioned BeWo culture media. Statistically differential proteins were determined using multiple testing correction (5% FDR). Differential proteins were ranked considering both the fold-change and the p-value for all dynamic comparisons. Volcano plots, heatmaps, and principal component analysis (PCA) plots were generated using Perseus [77].

Pathway enrichment and functional annotation analysis (DAVID) and hierarchical clustering heatmaps. Gene set enrichment analysis was conducted via GSEA database (https://www.gsea-msigdb.org/) and functional enrichment analysis was performed using the Database for Annotation, Visualization, and Integrated Discovery (DAVID) to identify overrepresented Gene Ontology (GO) categories, including biological processes [BP], cellular components [CC] and molecular functions [MF] (https://davidbioinformatics.nih.gov/). Pathway analyses were further conducted using the

Kyoto Encyclopedia of Genes and Genomes (KEGG) (https://www.genome.jp/kegg/pathway.html) and Reactome Pathway Database (https://reactome.org/) to elucidate the involvement of gene sets in specific biological pathways. These approaches provided insights into the functional roles and interactions of genes within the studied conditions. Heatmaps were generated in Python. Expression values from BeWo and MCF7 cells under static (S) and dynamic (D) conditions were averaged across the three biological replicates for each condition and transformed as $\log_2$(mean + 1). This approach stabilizes variation at low expression levels while preserving relative differences between conditions. Because BeWo and MCF7 are biologically distinct models, no cross-normalization was applied; the two cell lines were plotted side-by-side using their raw $\log_2$-scaled values. Heatmaps therefore represent absolute expression for static conditioned BeWo culture (BeWo-S), BeWo of dynamic PABC model (BeWo-D), static conditioned MCF7 culture (MCF7-S), MCF7 of dynamic PABC model (MCF7-D), with a dashed line marking the boundary between cell lines. A perceptual colormap with global scaling was used so color intensity reflects the underlying $\log_2$(mean + 1) expression values across the full dataset. Gene visualizations and pathway associations were constructed using Circos plot (https://circos.ca/). This tool enabled integrative mapping of gene relationships within the studied pathways.

Protein-protein interaction network construction. Protein–protein interaction networks were constructed using experimentally validated interactions retrieved from IMEx consortium databases, including IntAct, MINT, and MatrixDB. Network organization and centrality analysis were performed using Cytoscape software (https://cytoscape.org/) to highlight key regulatory proteins. Two networks were constructed for each cell environment comparison. First, a network with only the DEPs and interactions between them was constructed. For the dynamic versus static networks, a filtering step was applied to the list of DEPs where only DEPs identified in pathways clustered by DAVID were included. This allowed for a manageable construction of the PPI-Networks within Cytoscape, while maintaining the biological relevance of the list of DEPs. Second, an enriched network was created by extending the DEP-only network to include non-DEPs with at least one physical interaction with a DEP (first interactor non-DEPs). This enriched network was generated to better capture all the protein interactions underlying PABC. The main connected components of the DEP-only network and the enriched network were analyzed for each environment using topological measures such as degree (*k*) and closeness centrality (CC).

Immunofluorescence staining of the actin cytoskeleton & ZO-1 in BeWo cells and image analysis

To visualize ZO-1 tight junction and actin filaments, BeWo cells from the dynamic PABC model, the control dynamic BeWo model and static conditioned culture. Cells were fixed with 4% paraformaldehyde for 15 mins, permeabilized with 0.1% Triton™ X-100 (Sigma-

Aldrich, USA) and blocked with 5% bovine serum albumin (BSA; high grade; Sigma-Aldrich, USA). Cells were incubated with anti-ZO-1 polyclonal antibody (1:100 dilution; Invitrogen™, Life Technologies, Thermo Fisher Scientific, cat. no. 40-2200, USA) overnight at 4 °C, followed by washing once with PBS, and incubation with Alexa Fluor 647-conjugated secondary antibody (1:400 dilution; Invitrogen™, Life Technologies, Thermo Fisher Scientific, cat. no. A21245, USA) for 1 hour at room temperature. After washing with PBS, cells were incubated with Phalloidin (Invitrogen™, Life Technologies, Thermo Fisher Scientific, cat. no. A12379, USA) for 30 minutes, for visualization of actin filaments, then washing with PBS and incubation with DAPI (Invitrogen™, Thermo Fisher Scientific, cat. no. D1306, USA) for 10 minutes (1: 2500). Cells were imaged using Zeiss LSM900 Confocal microscope with 63X objective. Images were analyzed for nuclei counts and circularity using FIJI particle analysis function [78]. The intensity of the phalloidin, ZO-1, and DAPI stains were collected using FIJI. ZO-1 and phalloidin pockets were segmented using the Cellpose algorithm [79]. Actin stress fibrils organization on the surface of the phalloidin stain were evaluated using FibrilTool [80] in FIJI, which calculates a fiber anisotropy index (0 = isotropic, 1 = perfectly aligned fibers) and an angular variance. We compared anisotropy and angle variance between conditions to assess actin filament alignment. Statistical comparisons for imaging data were performed using Welch's t test with Holm–Šídák correction applied to account for multiple comparisons.

Functional validation of the PABC model with Coenzyme Q10 (CoQ10)

The dynamic PABC model was treated with Coenzyme Q10 (CoQ10) (≥98% HPLC, Sigma-Aldrich, cat. no. C9538, USA). CoQ10 was dissolved in dimethyl sulfoxide (DMSO, Invitrogen™, Thermo Fisher Scientific, cat. no. D12345, USA) to prepare a 20mM stock solution, which was further diluted in culture medium to achieve a final concentration of 10μM. We treated the dynamic PABC model with 10 μM of (CoQ10) under flow for 24 hours versus control untreated dynamic PABC model.

Western blot analysis of GRP78/HSPA5 marker & N-Cadherin-related proteins in MCF7 cell lysates

Total proteins were extracted using RIPA lysis buffer (Cell Signaling Technology, cat. no. 9806S, USA) according to the manufacturer's instructions. Equal amounts of total protein (20 μg), as determined by BCA assay, were loaded per lane of 4–12% Bis-Tris Plus WidgeWell gel (Invitrogen™, Thermo Fisher Scientific, cat. no. NW04122BOX, USA) and transferred onto polyvinylidene difluoride (PVDF) membranes (Thermo Scientific™, Thermo Fisher Scientific, cat. no. 88518, USA). Membranes were blocked with 5% (w/v) non-fat dry milk (BioShop Canada Inc., cat. no. SKI1400.500, Canada) prepared in phosphate-buffered saline (PBS) for 30 minutes at room temperature. Blocked membranes were incubated with anti-GRP78/HSPA5 (Bio-Techne, cat. no. MAB4846, USA) & anti-N Cadherin (Abcam, cat. no. AB98952-1001, USA) overnight at 4 °C

overnight. Membranes were then washed three times with tris buffer solution tween (TBST) and incubated with horseradish peroxidase (HRP)-conjugated goat anti-mouse secondary antibody (Abcam, cat. no. AB6789, USA) for 1 hour at room temperature. Finally, antibody-antigen complexes were visualized by enhanced chemiluminescence using prepared detection reagents (PBS, diaminobenzidine tetrahydrocholride and hydrogen peroxide). Band intensities were quantified and normalized to Ponceau S stain signal (Invitrogen™, Thermo Fisher Scientific, cat. no. A40000278, USA) and relative fold change was calculated against static and dynamic controls using Image Lab software (Bio-Rad Laboratories, USA). The lane profile tool was used to visualize signal intensity and optimize disc size for accurate quantification of target protein bands.

Enzyme-linked immunosorbent assay (ELISA) for latent TGFB1 in MCF7 cell lysates

Latent TGF-β1 in MCF7 cell lysates was quantified using TGF-β1 DuoSet ELISA kit (R&D Systems, Bio-Techne, cat. no. DY240-05, USA). Briefly, the capture antibody was coated onto the 96 well plate overnight at room temperature. Cell lysates (100 µL/well) were added and incubated for 2 hours. Detection antibody was then added and incubated for an additional 2 hours, followed by substrate addition for signal development. Absorbance was measured at 450 nm with 540/570 nm reference subtraction using a microplate reader Synergy™ H1 Hybrid Microplate Reader (Agilent BioTek Instruments, USA). Concentrations were determined from a standard curve generated with recombinant TGF-β1. Each sample was measured in duplicate. Statistical comparisons of latent TGF-β1 levels among conditions were performed using one-way ANOVA with Tukey's post hoc test.

Clinical data comparison for model validation

Breast Cancer Comparison. Statistical analysis of the clinical data was carried out using Python v3.11.4. Transcriptomic profiles of Breast invasive carcinoma tumours were downloaded from the TCGA-BRCA project (https://portal.gdc.cancer.gov/projects/TCGA-BRCA). Outlier profiles from the TCGA-BRCA dataset were identified and removed using ECOD (Empirical Cumulative Distribution-based Outlier Detection) and PCA. Remaining 1147 breast cancer profiles were analyzed. TPM values were then log2-transformed. The pyCombat package was used to remove batch effects between our data and the TCGA-BRCA dataset. Differential expression analysis between model-derived data and placental clinical samples was performed using a two-sided t-test, with statistical significance defined as $p < 0.05$.

Placenta Comparison. Placenta transcriptomic profiles were downloaded from the GEO database from a study conducting single-cell RNA-seq analysis on trophoblast subtypes (GSE89497) [20]. The mygene python package was used to convert Ensembl IDs to HGNC

IDs. The pyCombat package was used to remove batch effects between our data and the GSE31192 dataset. Differential expression analysis between model-derived data and placental clinical samples was performed using a two-sided t-test, with statistical significance defined as $p < 0.05$.

PABC Comparison. Transcriptomic profiles were downloaded from the GEO database (https://www.ncbi.nlm.nih.gov/geo/) from a study characterizing the molecular signature of PABC (GSE31192)[13]. The study contained 6 PABC patients with ER-positive tumors. Gene expression profiling from this study was carried out using Affymetrix U133 2plus Human Gene Chips. Ensembl Biomart (http://www.ensembl.org/biomart/martview/3c54fd6d8305088da303152173396ca7) was used to download a library of Affymetrix U133 2plus Human Gene Chip probe IDs to Ensembl IDs. The mygene python package was used to convert Ensembl IDs to HGNC IDs. The pyCombat package was used to remove batch effects between our data and the GSE31192 dataset. Differential expression analysis between model-derived data and placental clinical samples was performed using a two-sided t-test, with statistical significance defined as $p < 0.05$.

Statistical data analysis

Data are presented as mean ± standard deviation (SD) from at least three independent replicates. Statistical analyses were conducted in GraphPad Prism software (version 10.6; GraphPad Software, USA). For comparisons, we used Student's T-tests, using a two-tailed approach unless a one-tailed test was specified for a directional hypothesis. For comparisons with more than two groups, we applied one-way ANOVA, as appropriate. We then conducted Bonferroni's or Tukey's post hoc test to correct for multiple comparisons. We checked for normality and homoscedasticity. If the assumptions were violated, we used non-parametric tests. We considered a threshold of $p < 0.05$ to be statistically significant in all analyses. You can find the exact p values and specific tests used in the figure legends or the text when relevant.

Acknowledgment

H.I.L. acknowledges financial support from a CIHR Project Grant (NI22-1088R), the Natural Sciences and Engineering Research Council (NSERC Discovery Grant RGPIN-2020-05679), and St. Michael's Foundation, Unity Health Toronto (Angel's Den and Sara McComb Awards). Y.A. was supported by the Egyptian Mission Scholarship from the Egyptian Ministry of Higher Education. A.S.A. was supported by a scholarship from King Abdullah University of Science and Technology (KAUST Academy). M.A. was supported by the Lloyd and Marie Barbara PhD Scholarship from St. Michael's Foundation, Unity Health Toronto. R.R. was supported by a fellowship from the Data Science Institute (DSI)

at the University of Toronto. We thank Unity Health Core facilities for access to microscopy and molecular biology equipment. We also thank the Core Facility at the Department of Immunology, University of Manitoba, for access to flow cytometry and FACS, and Dr. Christine Zhang for technical support and training, including optimization of FACS parameters and sorting of samples into S- and M-phase populations.

Author Contributions

H.I.L. conceived the study. Y.A. and M.A. wrote the original draft. Y.A., M.A., H.A., R.P.Z., R.L., and H.I.L. reviewed and edited the manuscript. Y.A., M.A., P.P., and L.E. prepared the figures. Y.A., M.A., and H.I.L. contributed to methodology, investigation, formal analysis, validation, and data curation. R.R. performed validation and formal data analysis. P.P. performed PPI data analysis. M.K. and A.S.A. performed transcriptomics data analysis. Y.L. and R.P.Z. conducted secretomics and data analysis. Y.A., M.A., and H.I.L. acquired funding. H.I.L. supervised the project, provided resources, and administered the project.

Declaration of competing interest

The authors declare that they have no known competing financial interests or personal relationships that could have appeared to influence the work reported in this paper.

References

1 Smith, L., Bryan, S. & De, P. Canadian cancer statistics advisory committee. canadian cancer statistics 2018. *Can. Cancer Statist., Canada, Special Rep* (2018).

2 Navrozoglou, I. *et al.* Breast cancer during pregnancy: a mini-review. *Eur J Surg Oncol* **34**, 837-843, doi:10.1016/j.ejso.2008.01.029 (2008).

3 Kesireddy, M. & Krishnamurthy, J. Pregnancy-Associated Breast Cancer: Key Concepts for Optimizing Diagnosis and Treatment. *JCO Oncology Practice* **21**, 275-277, doi:10.1200/op-24-00867 (2025).

4 Zhang, Y., Yang, Z., Wang, C., Du, L. & Liu, Y. Pregnancy-associated breast cancer (PABC) in young women: a matched case-control study. *All Life* **16**, 2167867, doi:10.1080/26895293.2023.2167867 (2023).

5 Leslie, K. K., Koil, C. & Rayburn, W. F. Chemotherapeutic drugs in pregnancy. *Obstet Gynecol Clin North Am* **32**, 627-640, doi:10.1016/j.ogc.2005.08.009 (2005).

6 Cardonick, E. & Iacobucci, A. Use of chemotherapy during human pregnancy. *Lancet Oncol* **5**, 283-291, doi:10.1016/S1470-2045(04)01466-4 (2004).

7 Liu, F., Soares, M. J. & Audus, K. L. Permeability properties of monolayers of the human trophoblast cell line BeWo. *Am J Physiol* **273**, C1596-1604, doi:10.1152/ajpcell.1997.273.5.C1596 (1997).

8 Wice, B., Menton, D., Geuze, H. & Schwartz, A. L. Modulators of cyclic AMP metabolism induce syncytiotrophoblast formation in vitro. *Exp Cell Res* **186**, 306-316, doi:10.1016/0014-4827(90)90310-7 (1990).
9 Bode, C. J. *et al.* In vitro models for studying trophoblast transcellular transport. *Methods Mol Med* **122**, 225-239, doi:10.1385/1-59259-989-3:225 (2006).
10 Abostait, A. *et al.* Placental Nanoparticle Uptake-On-a-Chip: The Impact of Trophoblast Syncytialization and Shear Stress. *Molecular Pharmaceutics* **19**, 3757-3769, doi:10.1021/acs.molpharmaceut.2c00216 (2022).
11 Chen, C. H. *et al.* Characterization of the tumor immune microenvironment in pregnancy-associated breast cancer through multiplex immunohistochemistry and transcriptome analyses. *Breast Cancer Res* **27**, 154, doi:10.1186/s13058-025-02097-4 (2025).
12 Pena-Enriquez, R. *et al.* Molecular characterization of pregnancy-associated breast cancer and insights on timing from GEICAM-EMBARCAM study. *NPJ Breast Cancer* **11**, 12, doi:10.1038/s41523-025-00718-x (2025).
13 Harvell, D. M. *et al.* Genomic signatures of pregnancy-associated breast cancer epithelia and stroma and their regulation by estrogens and progesterone. *Horm Cancer* **4**, 140-153, doi:10.1007/s12672-013-0136-z (2013).
14 Bal Albayrak, M. G., Simsek, T., Akpinar, G., Kasap, M. & Canturk, N. Z. Proteomic insights into lymph node metastasis in breast cancer subtypes: Key biomarkers and pathways. *Pathol Res Pract* **269**, 155938, doi:10.1016/j.prp.2025.155938 (2025).
15 Xia, Q. *et al.* Disulfidptosis-associated lncRNAs predict breast cancer subtypes. *Sci Rep* **13**, 16268, doi:10.1038/s41598-023-43414-1 (2023).
16 Bathori, G., Csordas, G., Garcia-Perez, C., Davies, E. & Hajnoczky, G. Ca2+-dependent control of the permeability properties of the mitochondrial outer membrane and voltage-dependent anion-selective channel (VDAC). *J Biol Chem* **281**, 17347-17358, doi:10.1074/jbc.M600906200 (2006).
17 Baughman, J. M. *et al.* Integrative genomics identifies MCU as an essential component of the mitochondrial calcium uniporter. *Nature* **476**, 341-345, doi:10.1038/nature10234 (2011).
18 Di Sanzo, M., Quaresima, B., Biamonte, F., Palmieri, C. & Faniello, M. C. FTH1 Pseudogenes in Cancer and Cell Metabolism. *Cells* **9**, doi:10.3390/cells9122554 (2020).
19 Zhou, Q. *et al.* Ferroptosis in cancer: From molecular mechanisms to therapeutic strategies. *Signal Transduct Target Ther* **9**, 55, doi:10.1038/s41392-024-01769-5 (2024).
20 Liu, Y. *et al.* Single-cell RNA-seq reveals the diversity of trophoblast subtypes and patterns of differentiation in the human placenta. *Cell Res* **28**, 819-832, doi:10.1038/s41422-018-0066-y (2018).
21 Park, H. A. *et al.* Fluid shear stress enhances proliferation of breast cancer cells via downregulation of the c-subunit of the F(1)F(O) ATP synthase. *Biochem Biophys Res Commun* **632**, 173-180, doi:10.1016/j.bbrc.2022.09.084 (2022).
22 Chen, H.-A. *et al.* E1A-Mediated Inhibition of HSPA5 Suppresses Cell Migration and Invasion in Triple-Negative Breast Cancer. *Annals of surgical oncology* **22**, doi:10.1245/s10434-014-4061-3 (2014).

23 Direito, I. *et al.* The Clinicopathological Significance of BiP/GRP-78 in Breast Cancer: A Meta-Analysis of Public Datasets and Immunohistochemical Detection. *Curr Oncol* **29**, 9066-9087, doi:10.3390/curroncol29120710 (2022).

24 Song, T. *et al.* Small molecule inhibitor targeting the Hsp70-Bim protein-protein interaction in estrogen receptor-positive breast cancer overcomes tamoxifen resistance. *Breast Cancer Res* **26**, 33, doi:10.1186/s13058-024-01790-0 (2024).

25 Amaresan, R. & Gopal, U. Cell surface GRP78: a potential mechanism of therapeutic resistant tumors. *Cancer Cell Int* **23**, 100, doi:10.1186/s12935-023-02931-9 (2023).

26 Akinyemi, A. O. *et al.* Unveiling the dark side of glucose-regulated protein 78 (GRP78) in cancers and other human pathology: a systematic review. *Molecular Medicine* **29**, 112, doi:10.1186/s10020-023-00706-6 (2023).

27 Yu, H., Sun, C., Gong, Q. & Feng, D. Mitochondria-Associated Endoplasmic Reticulum Membranes in Breast Cancer. *Front Cell Dev Biol* **9**, 629669, doi:10.3389/fcell.2021.629669 (2021).

28 Hayashi, T. & Su, T. P. Sigma-1 receptor chaperones at the ER-mitochondrion interface regulate Ca(2+) signaling and cell survival. *Cell* **131**, 596-610, doi:10.1016/j.cell.2007.08.036 (2007).

29 Szabadkai, G. *et al.* Chaperone-mediated coupling of endoplasmic reticulum and mitochondrial Ca2+ channels. *J Cell Biol* **175**, 901-911, doi:10.1083/jcb.200608073 (2006).

30 Clendening, J. W. *et al.* Dysregulation of the mevalonate pathway promotes transformation. *Proc Natl Acad Sci U S A* **107**, 15051-15056, doi:10.1073/pnas.0910258107 (2010).

31 Centonze, G. *et al.* p140Cap modulates the mevalonate pathway decreasing cell migration and enhancing drug sensitivity in breast cancer cells. *Cell Death Dis* **14**, 849, doi:10.1038/s41419-023-06357-z (2023).

32 Korakiti, A. M., Moutafi, M., Zografos, E., Dimopoulos, M. A. & Zagouri, F. The Genomic Profile of Pregnancy-Associated Breast Cancer: A Systematic Review. *Front Oncol* **10**, 1773, doi:10.3389/fonc.2020.01773 (2020).

33 Wang, D. *et al.* Distinctive gene expression patterns in pregnancy-associated breast cancer. *Front Genet* **13**, 850195, doi:10.3389/fgene.2022.850195 (2022).

34 Zhang, J. *et al.* Identification of core genes and clinical roles in pregnancy-associated breast cancer based on integrated analysis of different microarray profile datasets. *Biosci Rep* **39**, doi:10.1042/BSR20190019 (2019).

35 Takeda, Y. *et al.* ROCK2 Regulates Monocyte Migration and Cell to Cell Adhesion in Vascular Endothelial Cells. *Int J Mol Sci* **20**, doi:10.3390/ijms20061331 (2019).

36 Wojciak-Stothard, B. & Ridley, A. J. Shear stress-induced endothelial cell polarization is mediated by Rho and Rac but not Cdc42 or PI 3-kinases. *J Cell Biol* **161**, 429-439, doi:10.1083/jcb.200210135 (2003).

37 Glasgow, E. & Mishra, L. Transforming growth factor-beta signaling and ubiquitinators in cancer. *Endocr Relat Cancer* **15**, 59-72, doi:10.1677/ERC-07-0168 (2008).

38 Zhou, F. *et al.* Nuclear receptor NR4A1 promotes breast cancer invasion and metastasis by activating TGF-beta signalling. *Nat Commun* **5**, 3388, doi:10.1038/ncomms4388 (2014).

39 Schioth, H. B., Roshanbin, S., Hagglund, M. G. & Fredriksson, R. Evolutionary origin of amino acid transporter families SLC32, SLC36 and SLC38 and physiological, pathological and therapeutic aspects. *Mol Aspects Med* **34**, 571-585, doi:10.1016/j.mam.2012.07.012 (2013).

40 Bodoy, S., Fotiadis, D., Stoeger, C., Kanai, Y. & Palacin, M. The small SLC43 family: facilitator system l amino acid transporters and the orphan EEG1. *Mol Aspects Med* **34**, 638-645, doi:10.1016/j.mam.2012.12.006 (2013).

41 Karahoda, R. *et al.* Trophoblast Differentiation Affects Crucial Nutritive Functions of Placental Membrane Transporters. *Front Cell Dev Biol* **10**, 820286, doi:10.3389/fcell.2022.820286 (2022).

42 Roberts, R. M. *et al.* Syncytins expressed in human placental trophoblast. *Placenta* **113**, 8-14, doi:10.1016/j.placenta.2021.01.006 (2021).

43 Xu, P. *et al.* Expression of matrix metalloproteinase-2, -9, and -14, tissue inhibitors of metalloproteinase-1, and matrix proteins in human placenta during the first trimester. *Biol Reprod* **62**, 988-994, doi:10.1095/biolreprod62.4.988 (2000).

44 Schedin, P. Pregnancy-associated breast cancer and metastasis. *Nat Rev Cancer* **6**, 281-291, doi:10.1038/nrc1839 (2006).

45 Nobes, C. D. & Hall, A. Rho, rac, and cdc42 GTPases regulate the assembly of multimolecular focal complexes associated with actin stress fibers, lamellipodia, and filopodia. *Cell* **81**, 53-62, doi:10.1016/0092-8674(95)90370-4 (1995).

46 Jansson, T., Castillo-Castrejon, M., Gupta, M. B., Powell, T. L. & Rosario, F. J. Down-regulation of placental Cdc42 and Rac1 links mTORC2 inhibition to decreased trophoblast amino acid transport in human intrauterine growth restriction. *Clin Sci (Lond)* **134**, 53-70, doi:10.1042/CS20190794 (2020).

47 Lamptey, J. *et al.* Downregulation of fascin in the first trimester placental villi is associated with early recurrent miscarriage. *Exp Cell Res* **403**, 112597, doi:10.1016/j.yexcr.2021.112597 (2021).

48 Timofeeva, A. V. *et al.* miRNAs and Their Gene Targets-A Clue to Differentiate Pregnancies with Small for Gestational Age Newborns, Intrauterine Growth Restriction, and Preeclampsia. *Diagnostics (Basel)* **11**, doi:10.3390/diagnostics11040729 (2021).

49 Gormley, M. *et al.* RNA profiling of laser microdissected human trophoblast subtypes at mid-gestation reveals a role for cannabinoid signaling in invasion. *Development* **148**, doi:10.1242/dev.199626 (2021).

50 Abid, N. *et al.* Regulation of stanniocalcin-1 secretion by BeWo cells and first trimester human placental tissue from normal pregnancies and those at increased risk of developing preeclampsia. *Faseb j* **34**, 6086-6098, doi:10.1096/fj.201902426R (2020).

51 Bishop, A., Cartwright, J. E. & Whitley, G. S. Stanniocalcin-1 in the female reproductive system and pregnancy. *Hum Reprod Update* **27**, 1098-1114, doi:10.1093/humupd/dmab028 (2021).

52 Walters, B. *et al.* Pregnancy-Associated Cancer: A Systematic Review and Meta-Analysis. *Mayo Clin Proc Innov Qual Outcomes* **8**, 188-199, doi:10.1016/j.mayocpiqo.2024.02.002 (2024).

53 Shechter Maor, G., Czuzoj-Shulman, N., Spence, A. R. & Abenhaim, H. A. Neonatal outcomes of pregnancy-associated breast cancer: Population-based study on 11 million births. *Breast J* **25**, 86-90, doi:10.1111/tbj.13156 (2019).
54 Lundberg, F. E., Gkekos, L., Rodriguez-Wallberg, K. A., Fredriksson, I. & Johansson, A. L. V. Risk of obstetric and perinatal complications in women presenting with breast cancer during pregnancy and the first year postpartum in Sweden 1973-2017: A population-based matched study. *Acta Obstet Gynecol Scand* **103**, 684-694, doi:10.1111/aogs.14555 (2024).
55 Bryant, C., Rawlinson, R. & Massey, A. J. Chk1 inhibition as a novel therapeutic strategy for treating triple-negative breast and ovarian cancers. *BMC Cancer* **14**, 570, doi:10.1186/1471-2407-14-570 (2014).
56 Pedram, A., Razandi, M., Evinger, A. J., Lee, E. & Levin, E. R. Estrogen inhibits ATR signaling to cell cycle checkpoints and DNA repair. *Mol Biol Cell* **20**, 3374-3389, doi:10.1091/mbc.e09-01-0085 (2009).
57 Doig, K. D., Fellowes, A. P. & Fox, S. B. Homologous Recombination Repair Deficiency: An Overview for Pathologists. *Mod Pathol* **36**, 100049, doi:10.1016/j.modpat.2022.100049 (2023).
58 Deng, C. X. BRCA1: cell cycle checkpoint, genetic instability, DNA damage response and cancer evolution. *Nucleic Acids Res* **34**, 1416-1426, doi:10.1093/nar/gkl010 (2006).
59 Cousineau, I., Abaji, C. & Belmaaza, A. BRCA1 regulates RAD51 function in response to DNA damage and suppresses spontaneous sister chromatid replication slippage: implications for sister chromatid cohesion, genome stability, and carcinogenesis. *Cancer Res* **65**, 11384-11391, doi:10.1158/0008-5472.CAN-05-2156 (2005).
60 Kwon, Y. *et al.* DNA binding and RAD51 engagement by the BRCA2 C-terminus orchestrate DNA repair and replication fork preservation. *Nat Commun* **14**, 432, doi:10.1038/s41467-023-36211-x (2023).
61 Shen, T., Vortmeyer, A. O., Zhuang, Z. & Tavassoli, F. A. High frequency of allelic loss of BRCA2 gene in pregnancy-associated breast carcinoma. *J Natl Cancer Inst* **91**, 1686-1687, doi:10.1093/jnci/91.19.1686 (1999).
62 Johannsson, O., Loman, N., Borg, A. & Olsson, H. Pregnancy-associated breast cancer in BRCA1 and BRCA2 germline mutation carriers. *Lancet* **352**, 1359-1360, doi:10.1016/S0140-6736(05)60750-7 (1998).
63 Ciciro, Y., Ragusa, D. & Sala, A. Expression of the checkpoint kinase BUB1 is a predictor of response to cancer therapies. *Sci Rep* **14**, 4461, doi:10.1038/s41598-024-55080-y (2024).
64 Lok, T. M. *et al.* Mitotic slippage is determined by p31(comet) and the weakening of the spindle-assembly checkpoint. *Oncogene* **39**, 2819-2834, doi:10.1038/s41388-020-1187-6 (2020).
65 Schrock, M. S., Stromberg, B. R., Scarberry, L. & Summers, M. K. APC/C ubiquitin ligase: Functions and mechanisms in tumorigenesis. *Semin Cancer Biol* **67**, 80-91, doi:10.1016/j.semcancer.2020.03.001 (2020).
66 Teran, E. *et al.* Coenzyme Q10 supplementation during pregnancy reduces the risk of pre-eclampsia. *Int J Gynaecol Obstet* **105**, 43-45, doi:10.1016/j.ijgo.2008.11.033 (2009).

67 Xu, X., Pan, J. R. & Zhang, Y. Z. CoQ10 alleviate preeclampsia symptoms by enhancing the function of mitochondria in the placenta of pregnant rats with preeclampsia. *Hypertens Pregnancy* **38**, 217-222, doi:10.1080/10641955.2019.1649420 (2019).

68 Sanz, G. *et al.* Differentiation of derived rabbit trophoblast stem cells under fluid shear stress to mimic the trophoblastic barrier. *Biochim Biophys Acta Gen Subj* **1863**, 1608-1618, doi:10.1016/j.bbagen.2019.07.003 (2019).

69 Deng, P. *et al.* Fluidic Flow Enhances the Differentiation of Placental Trophoblast-Like 3D Tissue from hiPSCs in a Perfused Macrofluidic Device. *Front Bioeng Biotechnol* **10**, 907104, doi:10.3389/fbioe.2022.907104 (2022).

70 Batut, B. *et al.* Community-Driven Data Analysis Training for Biology. *Cell Syst* **6**, 752-758 e751, doi:10.1016/j.cels.2018.05.012 (2018).

71 Hiltemann, S. *et al.* Galaxy Training: A powerful framework for teaching! *PLoS Comput Biol* **19**, e1010752, doi:10.1371/journal.pcbi.1010752 (2023).

72 Ewels, P., Magnusson, M., Lundin, S. & Kaller, M. MultiQC: summarize analysis results for multiple tools and samples in a single report. *Bioinformatics* **32**, 3047-3048, doi:10.1093/bioinformatics/btw354 (2016).

73 Martin, M. CUTADAPT removes adapter sequences from high-throughput sequencing reads. *EMBnet.journal* **17**, doi:10.14806/ej.17.1.200 (2011).

74 Dobin, A. *et al.* STAR: ultrafast universal RNA-seq aligner. *Bioinformatics* **29**, 15-21, doi:10.1093/bioinformatics/bts635 (2013).

75 Love, M. I., Huber, W. & Anders, S. Moderated estimation of fold change and dispersion for RNA-seq data with DESeq2. *Genome Biol* **15**, 550, doi:10.1186/s13059-014-0550-8 (2014).

76 Demichev, V., Messner, C. B., Vernardis, S. I., Lilley, K. S. & Ralser, M. DIA-NN: neural networks and interference correction enable deep proteome coverage in high throughput. *Nat Methods* **17**, 41-44, doi:10.1038/s41592-019-0638-x (2020).

77 Tyanova, S. *et al.* The Perseus computational platform for comprehensive analysis of (prote)omics data. *Nat Methods* **13**, 731-740, doi:10.1038/nmeth.3901 (2016).

78 Schindelin, J. *et al.* Fiji: an open-source platform for biological-image analysis. *Nat Methods* **9**, 676-682, doi:10.1038/nmeth.2019 (2012).

79 Stringer, C., Wang, T., Michaelos, M. & Pachitariu, M. Cellpose: a generalist algorithm for cellular segmentation. *Nat Methods* **18**, 100-106, doi:10.1038/s41592-020-01018-x (2021).

80 Boudaoud, A. *et al.* FibrilTool, an ImageJ plug-in to quantify fibrillar structures in raw microscopy images. *Nat Protoc* **9**, 457-463, doi:10.1038/nprot.2014.024 (2014).

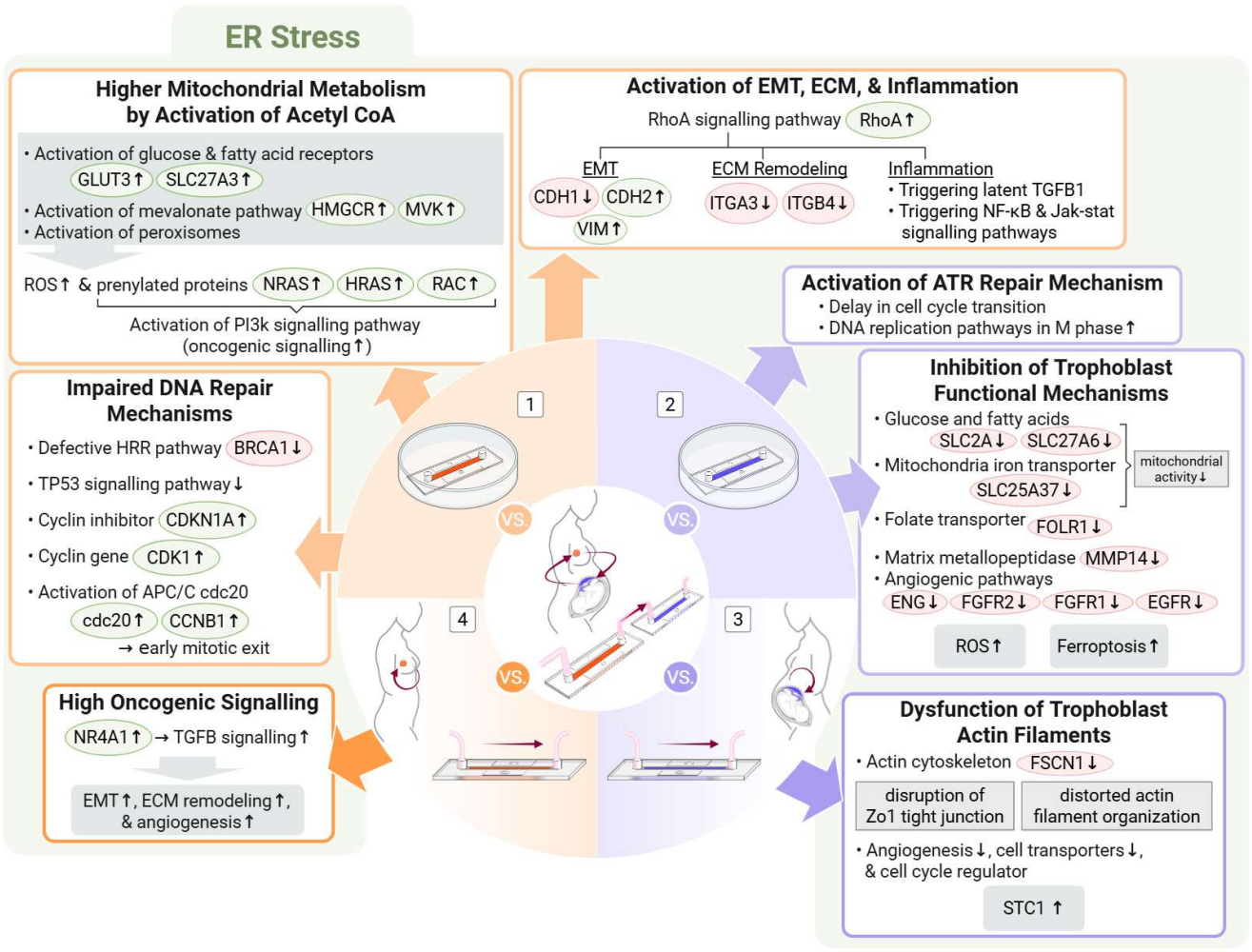


Fig. 1: Mechanistic overview of pathway alterations in PABC organ-on-a-chip model versus the different control conditions. The schematic summarizes the major pathway changes in the dynamic PABC model, in which MCF7 breast cancer cells (orange) and BeWo trophoblast cells (purple) are cultured on two microfluidic chips connected in tandem under continuous perfusion. The PABC model is compared against four controls: (1) Static conditioned MCF7 culture, (2) Static conditioned BeWo culture, (3) Control dynamic BeWo model, and (4) Control dynamic MCF7 model. Pathways and biological processes consistently up- or down-regulated in the dynamic PABC model are highlighted in the boxed panels. The diagram integrates transcriptomic and secretomic findings to depict how PABC model diverges from each control, and to outline the key mechanisms that define PABC biology.

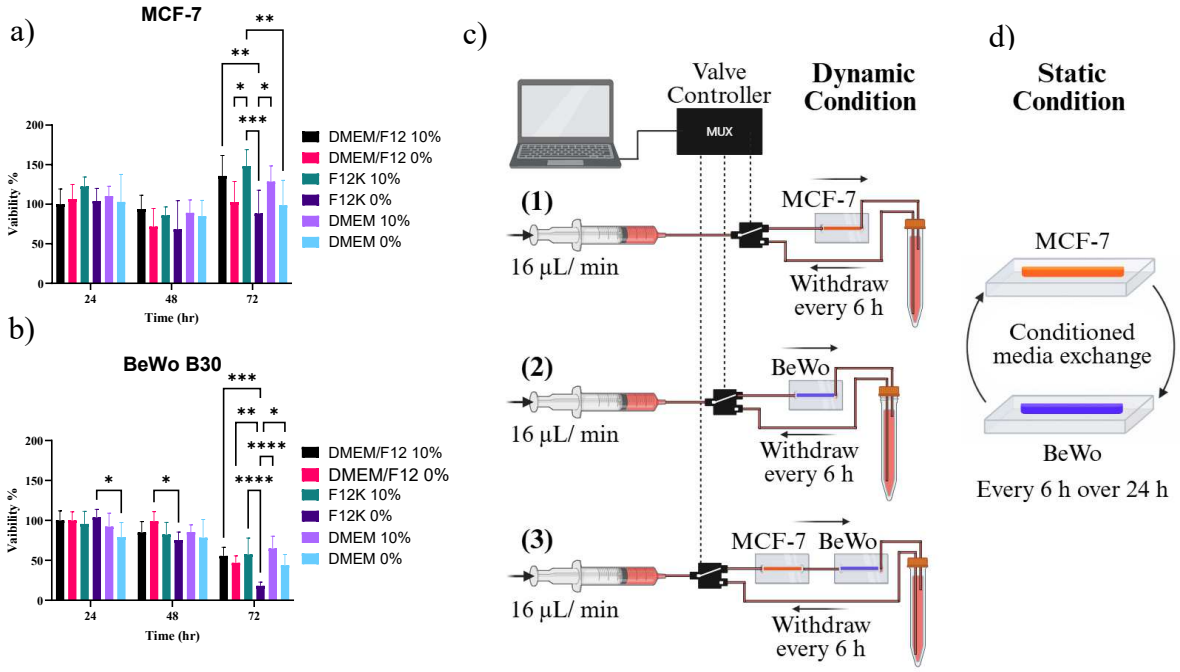


Fig. 2:Viability assay and dynamic recirculation setup for optimizing the dynamic PABC model.(a,b) Viability of (a) MCF7 and (b) BeWo B30 cells cultured in DMEM/F12, F12K, or DMEM, either serum-free media (SFM) or with 10% FBS, for 24, 48, and 72 hours (Calcein-AM staining; mean ± SD, n = 6). For MCF7 cells, two-way ANOVA showed significant effects of medium ($P < 0.0001$) and time ($P = 0.0004$) without interaction. For BeWo cells, both medium ($P < 0.0001$) and time ($P = 0.0005$) were significant, with interaction ($P = 0.0002$) due to time-dependent viability loss, notably in F12K SFM at 72 hours (Tukey's test, adjusted $P < 0.0001$). At 24 hours, both cell types maintained high viability (ranging from 80% to greater than 100%) across all media. DMEM/F12 SFM was selected as the shared perfusion medium for subsequent organ-on-chip studies .(c) Schematic of the dynamic-recirculation microfluidic system comprising syringe pumps (16 µL/min) and a MUX valve controller operating 3-way valves alternately directing flow toward the chips or to a second outlet for medium withdrawal every 6 hours to refill and reinfuse the circuit. Three parallel circuits were used: (1) MCF7, (2) BeWo, and (3) serial MCF7+BeWo. Medium: DMEM/F-12 SFM + 1% penicillin-streptomycin-neomycin. Tubing: PTFE. Arrows indicate flow direction; dashed lines represent digital valve control via MUX. (d) Static condition: conditioned-media exchange was done between MCF7 (orange) and BeWo (purple) chips, in which the medium collected from each chip is transferred to the other chip every 6 hours for 24 hours. This setup enables reciprocal paracrine signaling without flow-induced shear stress, serving as the static counterpart to the dynamic recirculation system.

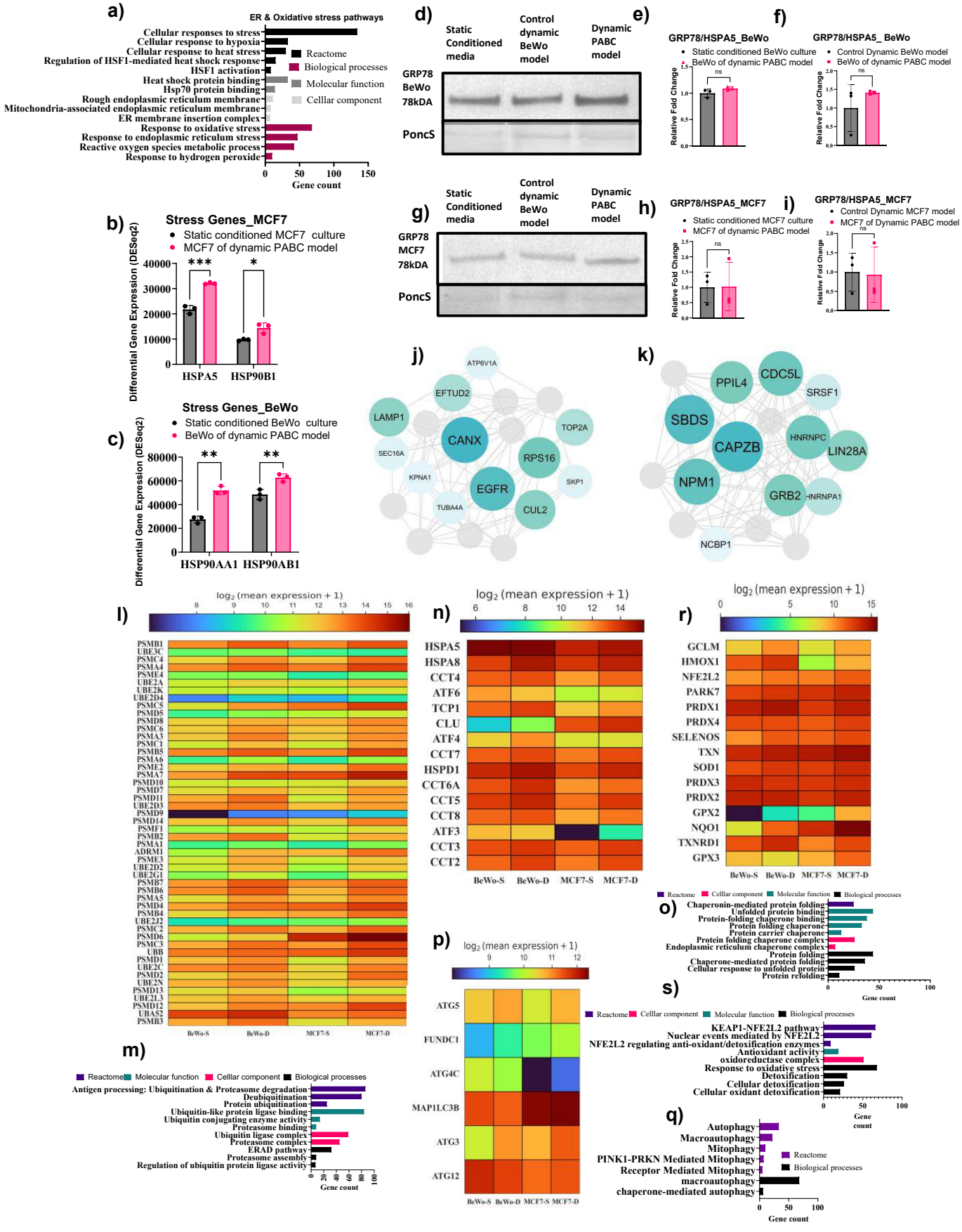

a)
ER & Oxidative stress pathways
Cellular responses to stress
Cellular response to hypoxia
Cellular response to heat stress
Regulation of HSF1-mediated heat shock response
HSF1 activation
Heat shock protein binding
Hsp70 protein binding
Rough endoplasmic reticulum membrane
Mitochondria-associated endoplasmic reticulum membrane
ER membrane insertion complex
Response to oxidative stress
Response to endoplasmic reticulum stress
Reactive oxygen species metabolic process
Response to hydrogen peroxide
Reactome
Biological processes
Molecular function
Celllar component
0
50
100
150
Gene count
b)
Stress Genes_MCF7
Static conditioned MCF7 culture
MCF7 of dynamic PABC model
Differential Gene Expression (DESeq2)
40000
30000
20000
10000
0
***
*
HSPA5
HSP90B1
c)
Stress Genes_BeWo
Static conditioned BeWo culture
BeWo of dynamic PABC model
Differential Gene Expression (DESeq2)
80000
60000
40000
20000
0
**
**
HSP90AA1
HSP90AB1
d)
Static Conditioned media
Control dynamic BeWo model
Dynamic PABC model
GRP78 BeWo 78kDA
PoncS
e)
f)
GRP78/HSPA5_BeWo
Static conditioned BeWo culture
BeWo of dynamic PABC model
Relative Fold Change
ns
GRP78/HSPA5_ BeWo
Control Dynamic BeWo model
BeWo of dynamic PABC model
Relative Fold Change
ns
g)
Static Conditioned media
Control dynamic BeWo model
Dynamic PABC model
GRP78 MCF7 78kDA
PoncS
h)
GRP78/HSPA5_MCF7
Static conditioned MCF7 culture
MCF7 of dynamic PABC model
Relative Fold Change
ns
i)
GRP78/HSPA5_MCF7
Control Dynamic MCF7 model
MCF7 of Dynamic PABC model
Relative Fold Change
ns
j)
ATP6V1A
EFTUD2
LAMP1
CANX
TOP2A
SEC16A
RPS16
KPNA1
EGFR
SKP1
TUBA4A
CUL2
k)
PPIL4
CDC5L
SRSF1
SBDS
CAPZB
HNRNPC
LIN28A
NPM1
GRB2
HNRNPA1
NCBP1
l)
log2 (mean expression + 1)
8
9
10
11
12
13
14
15
16
PSMB1
UBE3C
PSMC4
PSMA4
PSME4
UBE2A
UBE2K
UBE2D4
PSMC5
PSMD5
PSMD8
PSMC6
PSMA3
PSMC1
PSMB5
PSMA6
PSME2
PSMA7
PSMD10
PSMD7
PSMD11
UBE2D3
PSMD9
PSMD14
PSMF1
PSMB2
PSMA1
ADRM1
PSME3
UBE2D2
UBE2G1
PSMB7
PSMB6
PSMA5
PSMD4
PSMB4
UBE2J2
PSMC2
PSMD6
PSMC3
UBB
PSMD1
UBE2C
PSMD2
UBE2N
PSMD13
UBE2L3
PSMD12
UBA52
PSMB3
BeWo-S
BeWo-D
MCF7-S
MCF7-D
m)
Reactome
Molecular function
Celllar component
Biological processes
Antigen processing: Ubiquitination & Proteasome degradation
Deubiquitination
Protein ubiquitination
Ubiquitin-like protein ligase binding
Ubiquitin conjugating enzyme activity
Proteasome binding
Ubiquitin ligase complex
Proteasome complex
ERAD pathway
Proteasome assembly
Regulation of ubiquitin protein ligase activity
0
20
40
60
80
100
Gene count
n)
log2 (mean expression + 1)
6
8
10
12
14
HSPA5
HSPA8
CCT4
ATF6
TCP1
CLU
ATF4
CCT7
HSPD1
CCT6A
CCT5
CCT8
ATF3
CCT3
CCT2
BeWo-S
BeWo-D
MCF7-S
MCF7-D
p)
log2 (mean expression + 1)
9
10
11
12
ATG5
FUNDC1
ATG4C
MAP1LC3B
ATG3
ATG12
BeWo-S
BeWo-D
MCF7-S
MCF7-D
r)
log2 (mean expression + 1)
0
5
10
15
GCLM
HMOX1
NFE2L2
PARK7
PRDX1
PRDX4
SELENOS
TXN
SOD1
PRDX3
PRDX2
GPX2
NQO1
TXNRD1
GPX3
BeWo-S
BeWo-D
MCF7-S
MCF7-D
o)
Reactome
Celllar component
Molecular function
Biological processes
Chaperonin-mediated protein folding
Unfolded protein binding
Protein-folding chaperone binding
Protein folding chaperone
Protein carrier chaperone
Protein folding chaperone complex
Endoplasmic reticulum chaperone complex
Protein folding
Chaperone-mediated protein folding
Cellular response to unfolded protein
Protein refolding
0
50
100
Gene count
s)
Reactome
Celllar component
Molecular function
Biological processes
KEAP1-NFE2L2 pathway
Nuclear events mediated by NFE2L2
NFE2L2 regulating anti-oxidant/detoxification enzymes
Antioxidant activity
oxidoreductase complex
Response to oxidative stress
Detoxification
Cellular detoxification
Cellular oxidant detoxification
0
50
100
Gene count
q)
Autophagy
Macroautophagy
Mitophagy
PINK1-PRKN Mediated Mitophagy
Receptor Mediated Mitophagy
macroautophagy
chaperone-mediated autophagy
Reactome
Biological processes
0
50
100
Gene count

Fig. 3: Activation of endoplasmic-reticulum (ER) stress, unfolded protein response and ubiquitin activity, autophagy and redox-regulatory pathways under dynamic PABC model. a) GO (BP/CC/MF) and Reactome enrichment highlight activation of ER- and oxidative-stress pathways, including response to oxidative stress, ER stress, HSF1-mediated heat-shock response and hypoxia.(b,c) Differential expression shows HSPA5, HSP90B1 in MCF7 ($P = 0.0007, 0.0157$) and upregulation of HSP90AA1, HSP90AB1 in BeWo ($P = 0.0013, 0.0096$) under dynamic PABC model versus static conditioned cultures (unpaired two-tailed t-test, Holm–Šídák correction). Bars show mean ± s.d.; $P < 0.05$, $P < 0.01$, $P < 0.001$.(d-i) GRP78/HSPA5 validation. (d-i) Western blot analysis for media of BeWo and MCF7 under dynamic PABC model (20µg loaded per lane and normalized to Ponceau stain), showing GRP78 at 78kDa where band intensity was normalized to control either static or control dynamic. BeWo of dynamic PABC model showed higher relative fold change compared to control dynamic BeWo model and an increase compared to static BeWo conditioned culture which was not statistically significant. While MCF7 of dynamic PABC model showed no statistically significant difference. bars show mean ± s.d. (j) PPI network shows CANX protein which is upregulated protein with highest degree of connectivity (k=256). (k) PPI network shows CAPZB protein to be downregulated with a degree of connectivity k=455, where DEPs are colored according to their degree, while the surrounding gray nodes represent the 5–10 highest-degree interacting non-DEPs proteins within the network. (l–s) Heatmaps and enrichment analyses demonstrate activation of the ubiquitin–proteasome system (UPS), UPR, ER-associated degradation (ERAD), autophagy/mitophagy, and antioxidant responses, including KEAP1–NFE2L2 signaling. Heatmaps (l, n, r, p): show $\log_2$ (mean expression + 1) from three biological replicates per condition BeWo-S (static conditioned BeWo culture), BeWo-D (dynamic PABC model), MCF7-S (static conditioned MCF7 culture), MCF7-D (dynamic PABC model). Color scale represents absolute $\log_2$ expression (warmer = higher expression). Statistics (b,c): unpaired two-tailed t-tests with Holm–Šídák correction.

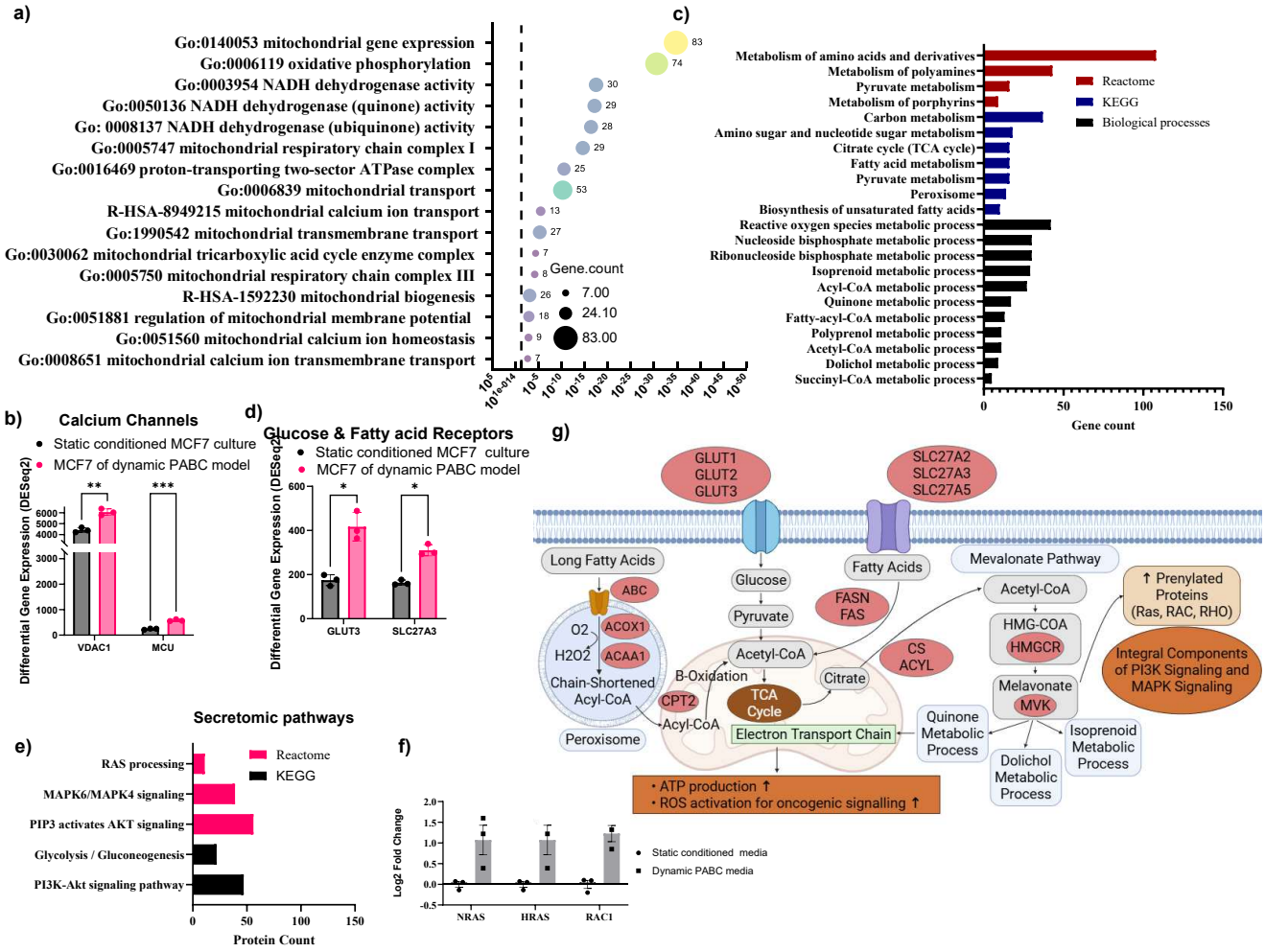


Fig. 4: Mitochondrial Metabolic Pathways and Acetyl-CoA Activation Network in MCF7 cells in the dynamic PABC model versus static conditioned MCF7 culture. (a)Gene Ontology and Reactome analyses (via DAVID) showed upregulation of mitochondrial pathways, including biogenesis, electron transport chain, TCA cycle, and calcium homeostasis under dynamic flow. (b) Calcium-channel genes VDAC1 and MCU were significantly upregulated at S phase (P = 0.0022 and P = 0.0010, respectively; unpaired t-test with Welch's correction, Holm–Šídák adjustment). (c) Enrichment of acetyl-CoA–related metabolic pathways, including pyruvate and fatty acid metabolism, alongside isoprenoid and quinone biosynthesis. (d) GLUT3 and SLC27A3 were significantly upregulated (P = 0.003711 and P = 0.000812, respectively; unpaired t-test with Welch's correction, Holm–Šídák adjustment). (e,f) Secretome analysis indicating activation of RAS processing and downstream PI3K–Akt and MAPK signaling, supported by higher log2 fold change of NRAS, HRAS, and RAC1.(g) Schematic illustration summarizing mitochondrial and acetyl CoA activation via integration of glucose and fatty-acid metabolism, mevalonate pathway and peroxisomal activation, with downstream effects on ATP production, ROS generation, and oncogenic signaling through PI3K/MAPK pathways. Data are mean ± s.d.; statistical significance determined by unpaired t-test with Holm–Šídák correction (*P < 0.05, **P < 0.01, ***P < 0.001)

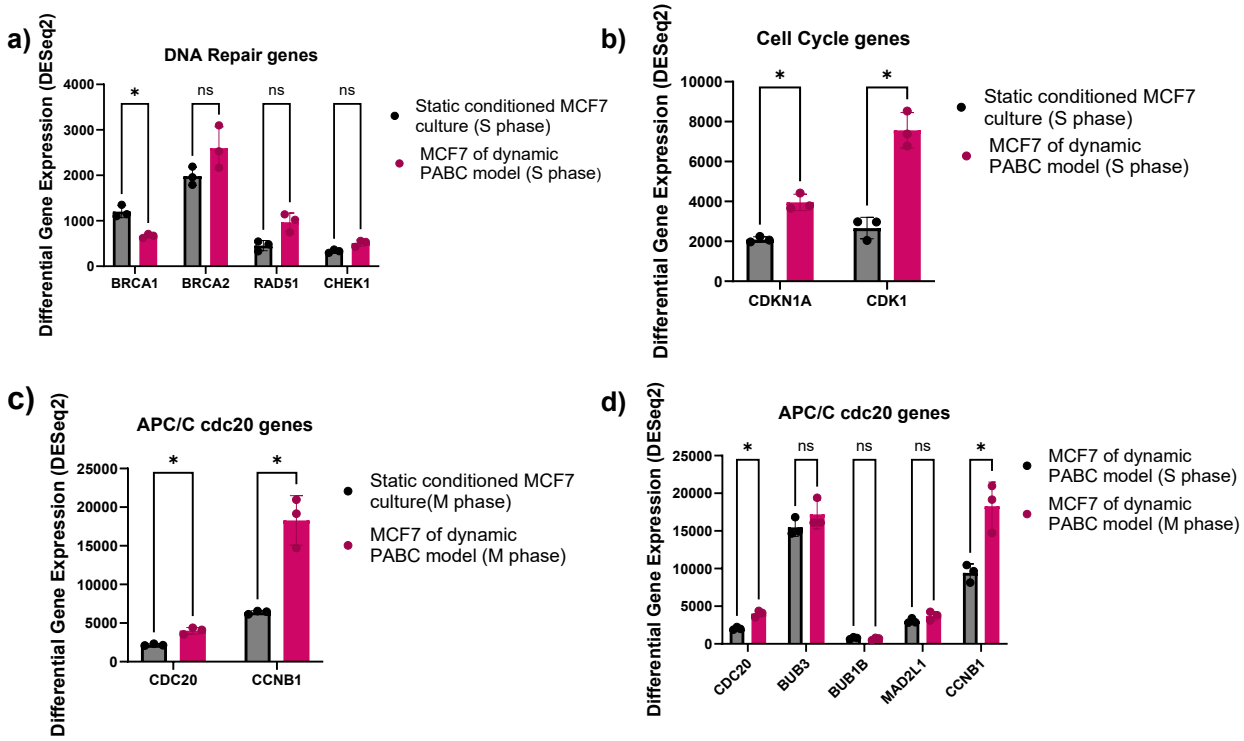


Fig. 5: Expression profiles of DNA Repair, cell cycle regulator and APC/C–CDC20 Regulatory Genes. (a) DNA repair gene BRCA1 showed significant downregulation in MCF7 in the dynamic PABC model (S phase) compared to static conditioned MCF7 culture (S phase) (P =0.002809), while BRCA2, RAD51 and CHEK1 doesn't show statistical significant difference, the data demonstrated a consistent trend toward increased mean expression. (b) cyclin inhibitor CDKN1A and cyclin gene CDK1 showed a significant upregulation (P=0.001678 and P=0.001230 respectively) in MCF7 of the dynamic PABC model (S phase) compared to static conditioned MCF7 culture (S phase). (c) significant upregulation of CDC20 and CCNB1 of APC/C complex at M phase in MCF7 of dynamic PABC model compared to static conditioned MCF7 culture (P=0.002161 and P=0.003072 respectively). (d) CDC20 and CCNB1 showed statistical significance between S and M phase of MCF7 in the dynamic PABC model (P= 0.001960 and P=0.011008 respectively) while mitotic checkpoint complex genes (BUB3, BUB1B and MAD2L1) showed no statistical difference with similar expression pattern between S and M phases of MCF7 in the dynamic PABC model. Statistical significance was determined using t-tests with Holm–Šidák correction for multiple comparisons. Data are represented as mean ± SD from three independent biological replicates.

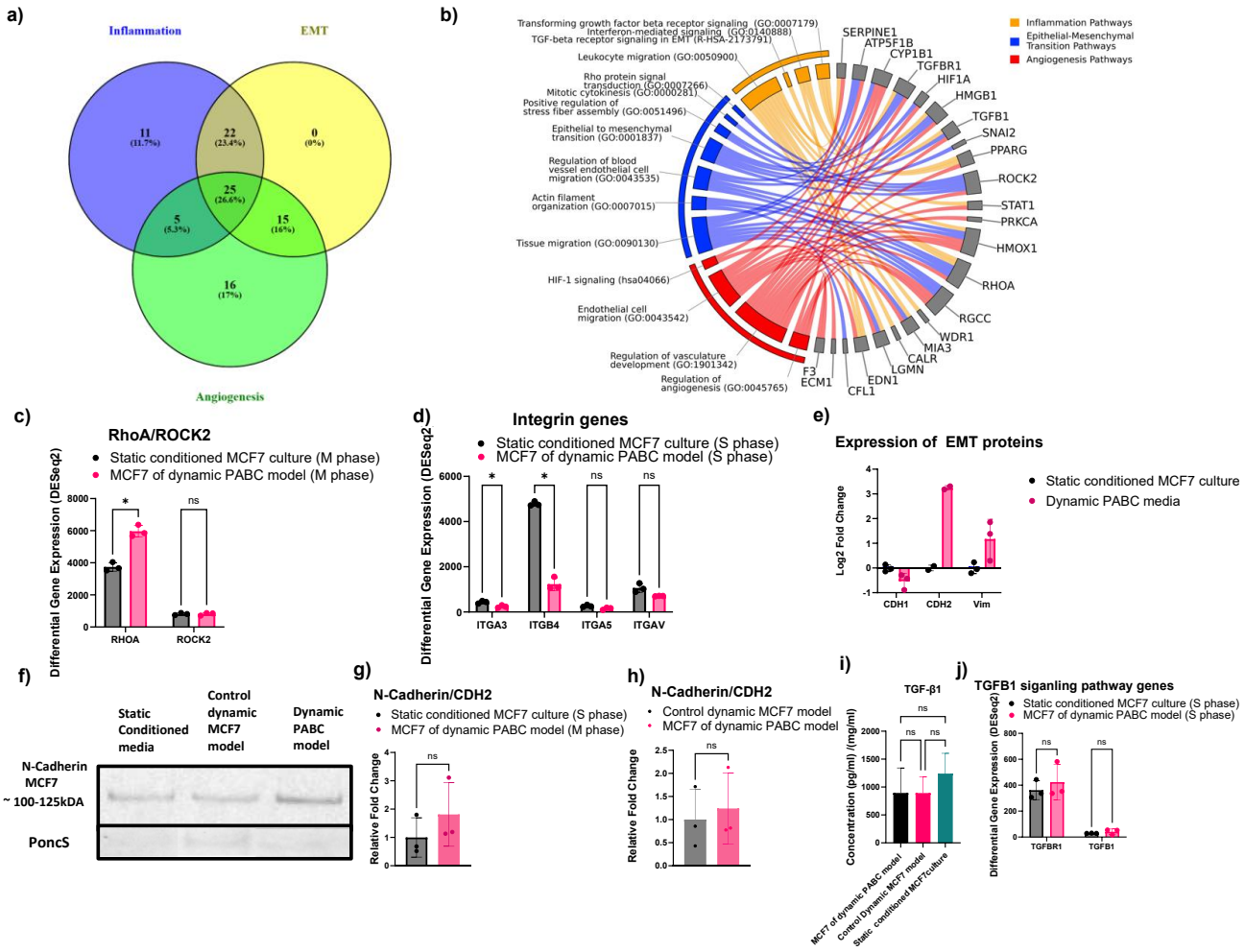


Fig. 6: Cross-talk between inflammation, EMT, and angiogenesis pathways in MCF7 cells in the dynamic PABC model I. (a) Venn diagram showing overlap of differentially expressed genes (b) Circos plot linking the 25 shared genes to enriched pathways, including Rho signaling, TGFB signaling, stress fiber assembly, actin assembly, EMT and angiogenesis.(c) Expression analysis of RHoA and ROCK2; RHoA was significantly upregulated in the dynamic model (p= 0.003), while ROCK2 showed no change.(d) Integrin expression where ITGA3 and ITGB4 were statistically significantly downregulated (p=0.013833 and p=0.000782 respectively) and ITGA5 and ITGAV did not differ significantly between static conditioned MCF7 culture and MCF7 cells in the dynamic PABC model (S phase). (e) Secretome analysis revealed log2 fold downregulation of E-Cadherin -0.53 (CDH1) and increased log2 fold change of N-Cadherin (CDH2) and vimentin (Vim), with fold changes 3.24 (two-points) and 1.17, respectively, in the dynamic PABC media. (f-h) Western blot showing stronger N-cadherin (CDH2) expression (20µg loaded per lane and normalized to Ponceau signal) where relative fold change was higher in MCF7 cells of the dynamic PABC model compared with static conditioned MCF7 culture and control dynamic MCF7 model. bars show mean ± s.d. (i) ELISA for latent TGF-β1 showed higher secretion in the static conditioned culture compared with dynamic PABC model and control dynamic MCF7 model ; One way ANOVA confirmed no significant difference across groups.(j) Gene expression of TGF-β1 and TGFBR1 also showed no statistical difference between static and dynamic conditions while an overall increase in mean expression was observed. Data shown as mean ± SD. Statistical testing used Welch's t test with Holm–Šídák correction (α = 0.05) or one-way ANOVA with multiple-comparison correction where appropriate.

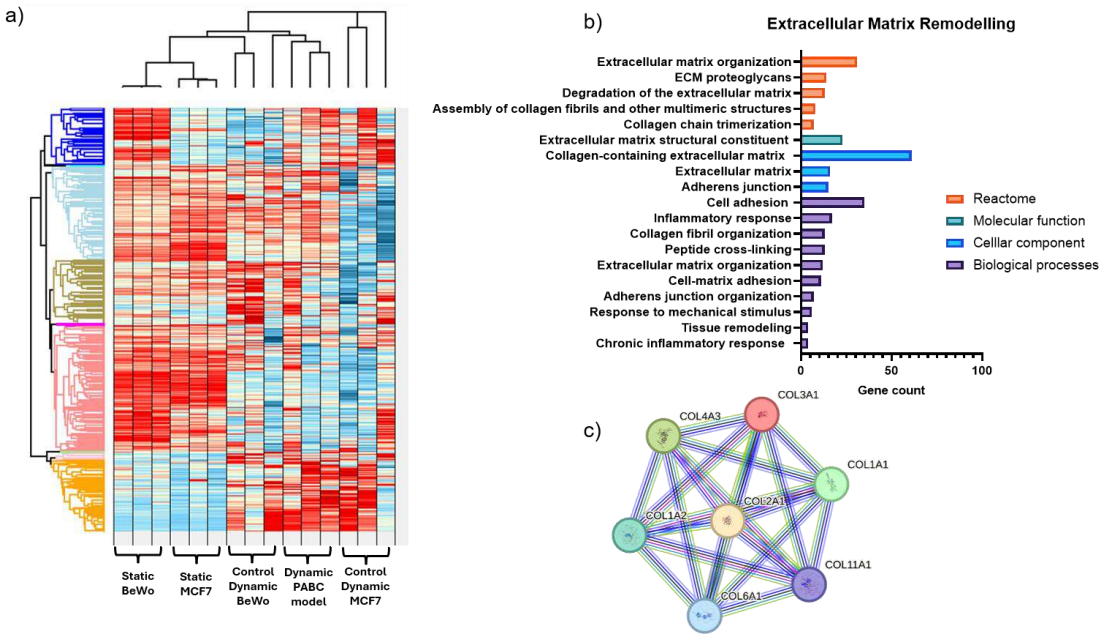


Fig. 7: Remodeling of extracellular matrix milieu. (a) Heatmap clustering of secreted proteins from the secretomic analysis identified nine distinct protein expression clusters. (b) GO enrichment analysis covering BP, CC, and MF along with Reactome pathway analysis of upregulated proteins in the dynamic PABC model compared to the static conditioned model, revealed enrichment in ECM remodeling, adherens junction organization, mechanical stress response, and inflammatory signaling pathways. (c) STRING (PPI) network analysis highlighted a collagen-associated cluster composed of COL1A1, COL1A2, COL2A1, COL3A1, COL4A3, COL6A1, and COL11A1, as components of ECM remodeling.

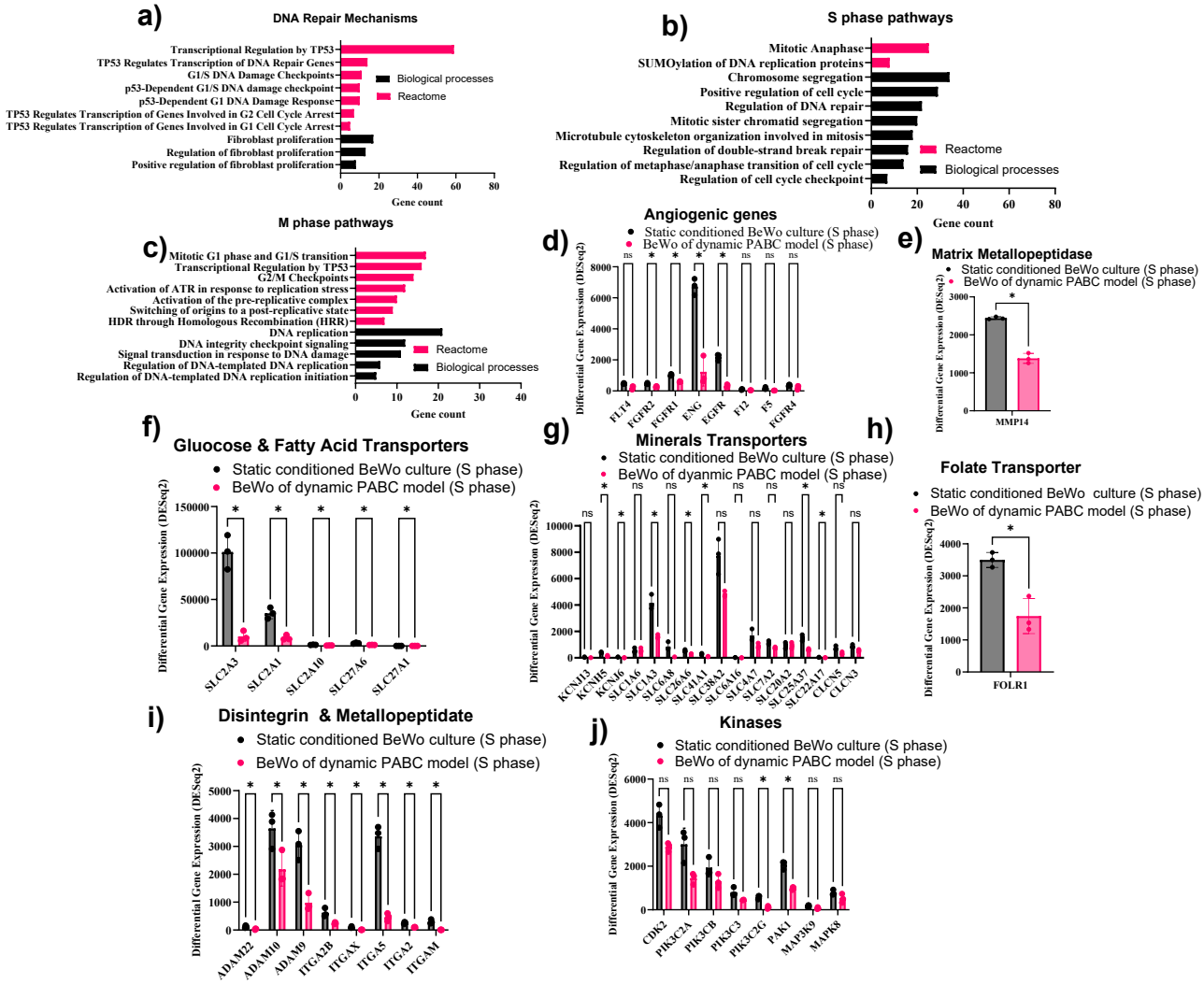


Fig. 8: DNA repair mechanisms & Expression profile of angiogenic genes, cell transporters, kinases and matrix metallopeptidase genes in BeWo cells of the dynamic PABC model. (a) Pathway analysis indicated activation of DNA repair and TP53-related programs (b), enrichment of mitotic and DNA repair pathways during S phase (c) Persistent activation of DNA replication pathways during M phase.(d) Among angiogenic genes, FGFR1, FGFR2, ENG, and EGFR were significantly reduced in the dynamic BeWo model versus static conditioned BeWo culture (P=0.001413, P=0.008611, P=0.002228 and P=0.001103) respectively. In contrast, others, such as FLT4 and FGFR4, did not differ. (e) The matrix metalloproteinase MMP14 was significantly downregulated (P=0.003368). (f) Glucose and fatty acid transporters (SLC2A1, SLC2A3, SLC2A10, SLC27A6 and SLC27A1) were all significantly downregulated (P=0.007462, P=0.008646, P=0.004833, P=0.019932 and P=0.00773) respectively. (g) For mineral transporters, KCNH5 and KCNJ6 were significantly downregulated (P=0.001311and P=0.002012) respectively, SLC1A3, SLC26A6 and SLC41A1 were significantly downregulated (P=0.001629, P=0.003224 and P=0.001697) respectively besides SLC25A37 and SLC22A17 (P=0.003081 and P=0.003708) respectively; the remainder were unchanged. (h) The folate transporter FOLR1 was also significantly downregulated (P=0.007029). (j) Disintegrin and metallopeptidase genes showed significant downregulation ADAM2 (P=0.024701), ADAM10 (P=0.045505), ADAM9 (P=0.004010), ITGA2B (P=0.015098), ITGAX (P=0.003080), ITGA5 (P=0.000305), ITGA2 (P=0.001457) and ITGAM (P=0.002343). (j) Within kinase pathways, PIK3C2G and PAK1 were significantly lower (P=0.001484, P=0.000742), while changes in CDK2, other PI3Ks, and MAP

kinases were not significant. Values are mean ± SD. Statistics were performed using Welch's t test with Holm–Šídák correction for multiple comparisons (α = 0.05).

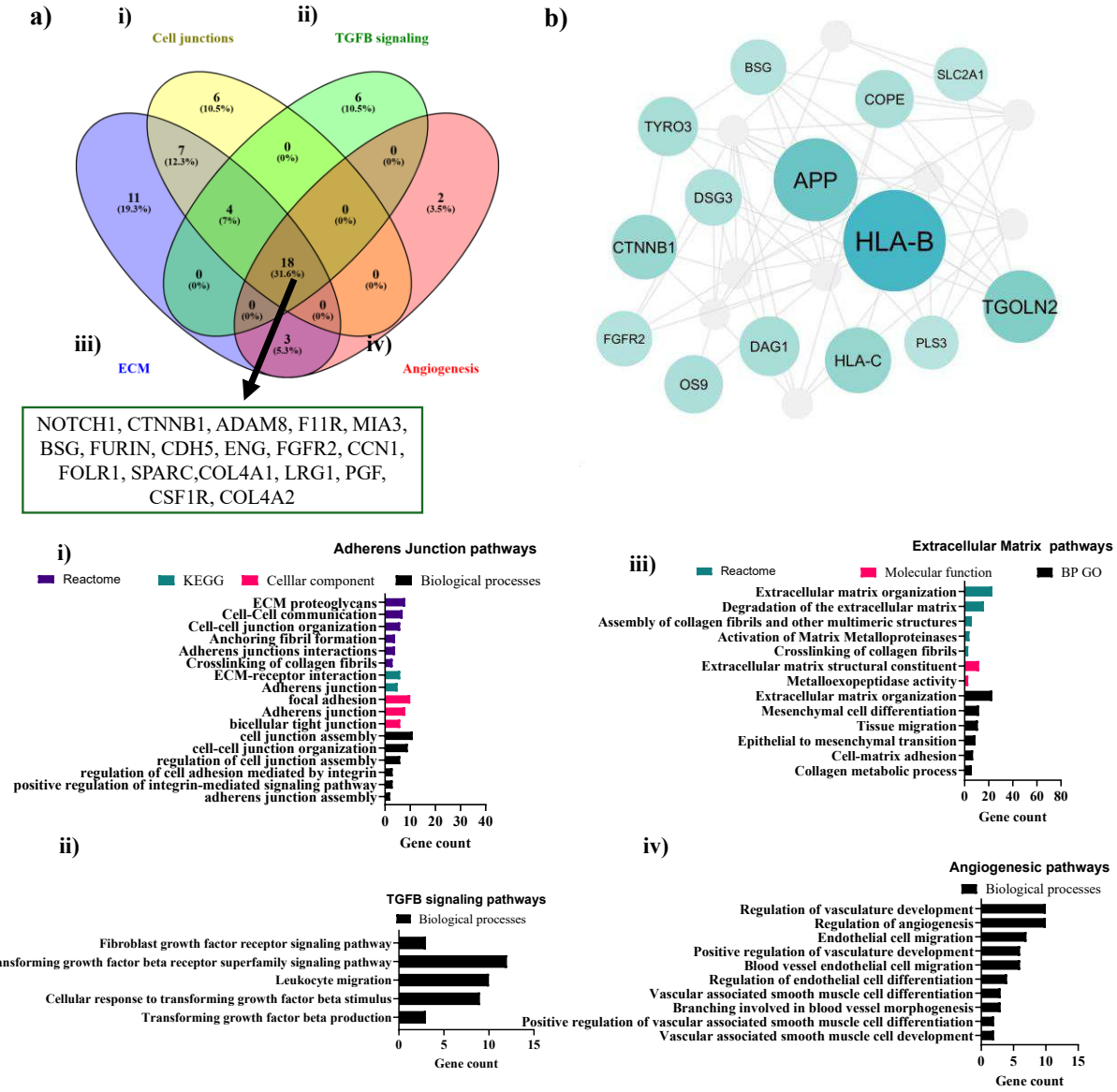


Fig. 9: Enriched secreted protein pathways in dynamic PABC model versus breast cancer model. (a) Pathway overlap analysis by Venn diagram shows the overlap of secreted proteins identified within four enriched functional categories: (i) cell junctions, (ii) TGF-β signaling, (iii) ECM organization, and (iv) angiogenesis. Eighteen proteins (31.6%) were shared across all categories, representing a core subset involved in structural organization, growth-factor signaling, and vascular regulation. (i–iv) highlight representative GO, KEGG and Reactome terms associated with adherens junctions, TGF-β signaling, ECM remodeling, and angiogenesis.(b) PPI network shows HLA-B and APP proteins shows highest degree of connectivity (k=144) and (k=95) respectively, where DEPs are colored according to their degree, while the surrounding gray nodes represent the 5–10 highest-degree interacting non-DEPs proteins within the network.

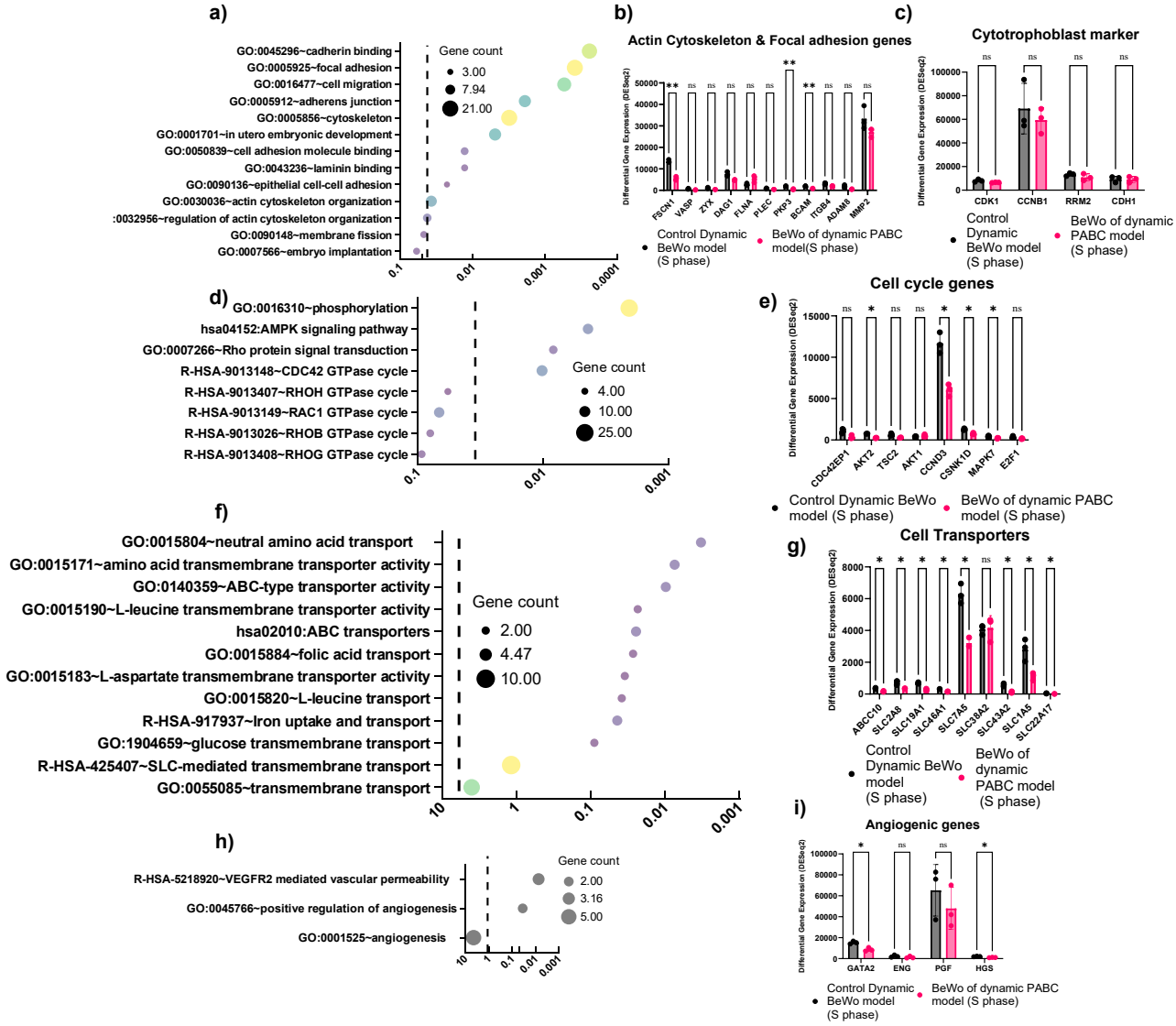


Fig. 10: Inhibition of cell Transport, angiogenesis, cell cycle, and cytoskeleton mechanisms in BeWo cells of the dynamic PABC model. Gene Ontology (GO) and Reactome enrichment bubble plots showing pathways in BeWo cells cultured in dynamic PABC model in relative to control dynamic BeWo model. In all plots, the x-axis represents P-values on a reversed log scale, with pathways to the right of the dashed line (P = 0.05) significantly enriched; bubble size indicates the number of genes per pathway. (a) Actin-cytoskeleton and focal-adhesion processes were significantly downregulated. (b)Bar chart showed significant downregulation of FSCN1, PKP3 and BCAM (P=0.0003, P=0.0007 and P=0.0002) respectively. (c) Cytotrophoblast markers remained stable. (d) Cell-cycle-related pathways involving phosphorylation, RAC1 GTPase cycle, CDC42 GTPase cycle, AMPK, AKT and Rho-GTPase signaling were downregulated. (e) Bar chart showed significant downregulation of cell cycle, growth and proliferative genes which include AKT2, CCND3, CSNK1D and MAPK7 genes (P<0.0001, P=0.0026, P=0.0026 and P=0.0089) respectively. (f) Cell-transport pathways were inhibited. (g)Bar graph showed representative transporters with significantly lower expression of organic iron transporter ABCC10 (P=0.000633), glucose transporter SLC2A8 (P=0.008722), folic acid transporters SLC19A1 and SLC46A1 (P=0.000495 and P=0.000904), amino acid transport SLC1A5 (P=0.016389), Na+-independent large amino acids SLC7A5 (P=0.001550). (h) Angiogenic pathways such as VEGFR2-mediated vascular permeability and positive regulation of angiogenesis were downregulated. (i) Significant lower expression of pro-angiogenic mediators including GATA2 and HGS (P=0.006470 and P=0.004110) respectively. Statistical comparisons were made using

unpaired two-tailed t-tests (Welch's correction when required) with Holm–Šídák or FDR adjustment (α = 0.05). Significance: P < 0.05 = *, < 0.01 = **, < 0.001 = ***, < 0.0001 = ****; ns, not significant.

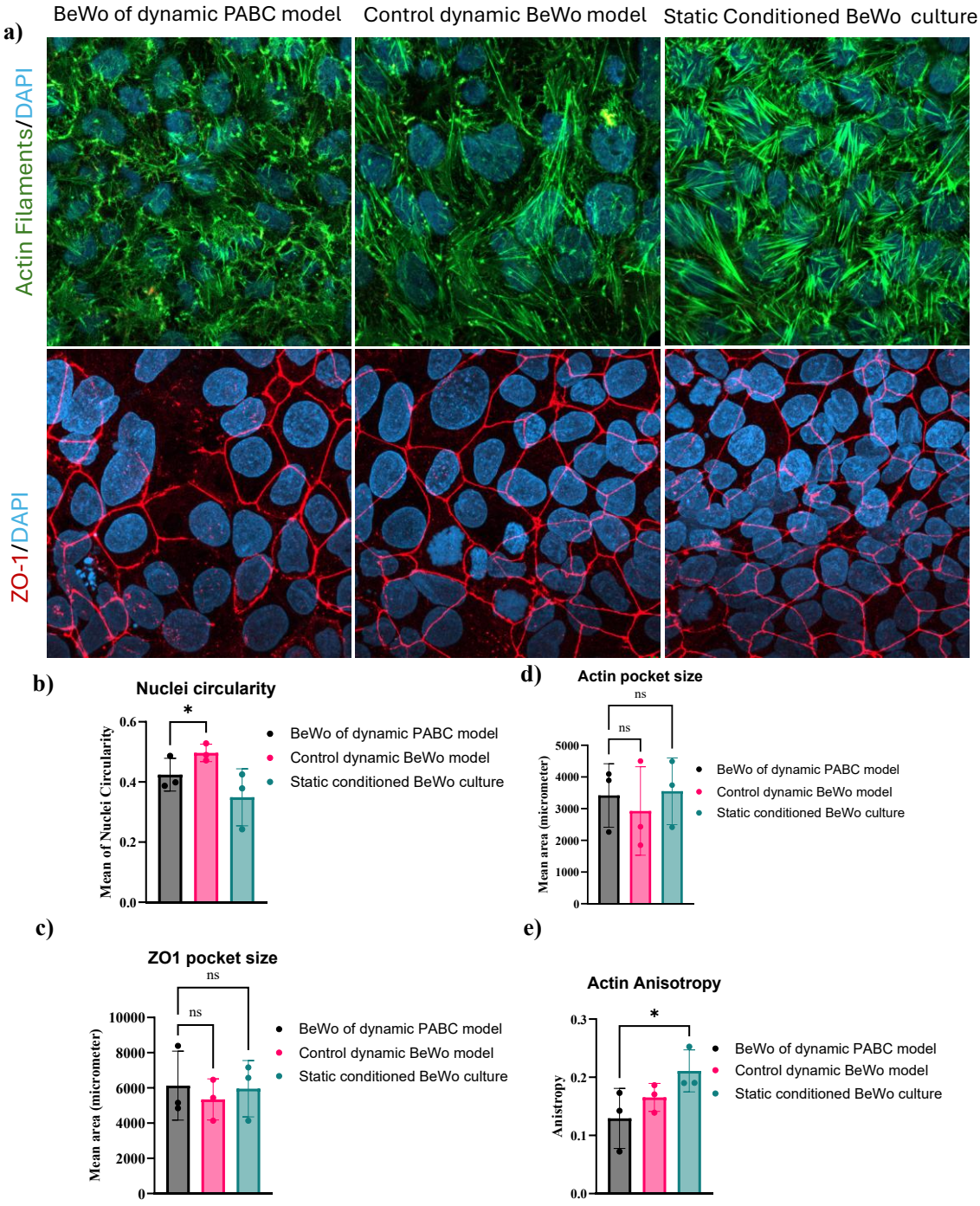


Fig. 11: Cytoskeletal architecture and junctional organization in BeWo (a) Confocal images: F-actin (phalloidin, green), ZO-1 (red), nuclei (DAPI, blue). (b) Nuclear circularity: higher in control dynamic BeWo model vs BeWo cells of the dynamic PABC model (paired one-tailed t-test on matched samples, n=3 pairs, P=0.0266). (c) ZO-1 pocket area: no difference (one-way ANOVA, P=0.827; all pairwise tests ns). (d) Actin pocket area: no difference across conditions (one-way ANOVA, P=0.794; Šídák post hoc: BeWo dynamic PABC model vs control dynamic BeWo model P=0.817; BeWo dynamic PABC model vs static conditioned BeWo cultures P=0.990; both ns).(e) Actin anisotropy: statistically significant lower in the dynamic PABC model vs static conditioned BeWo culture (mean ± SD; n = 3 per group; unpaired one-tailed t-test, P=0.044).

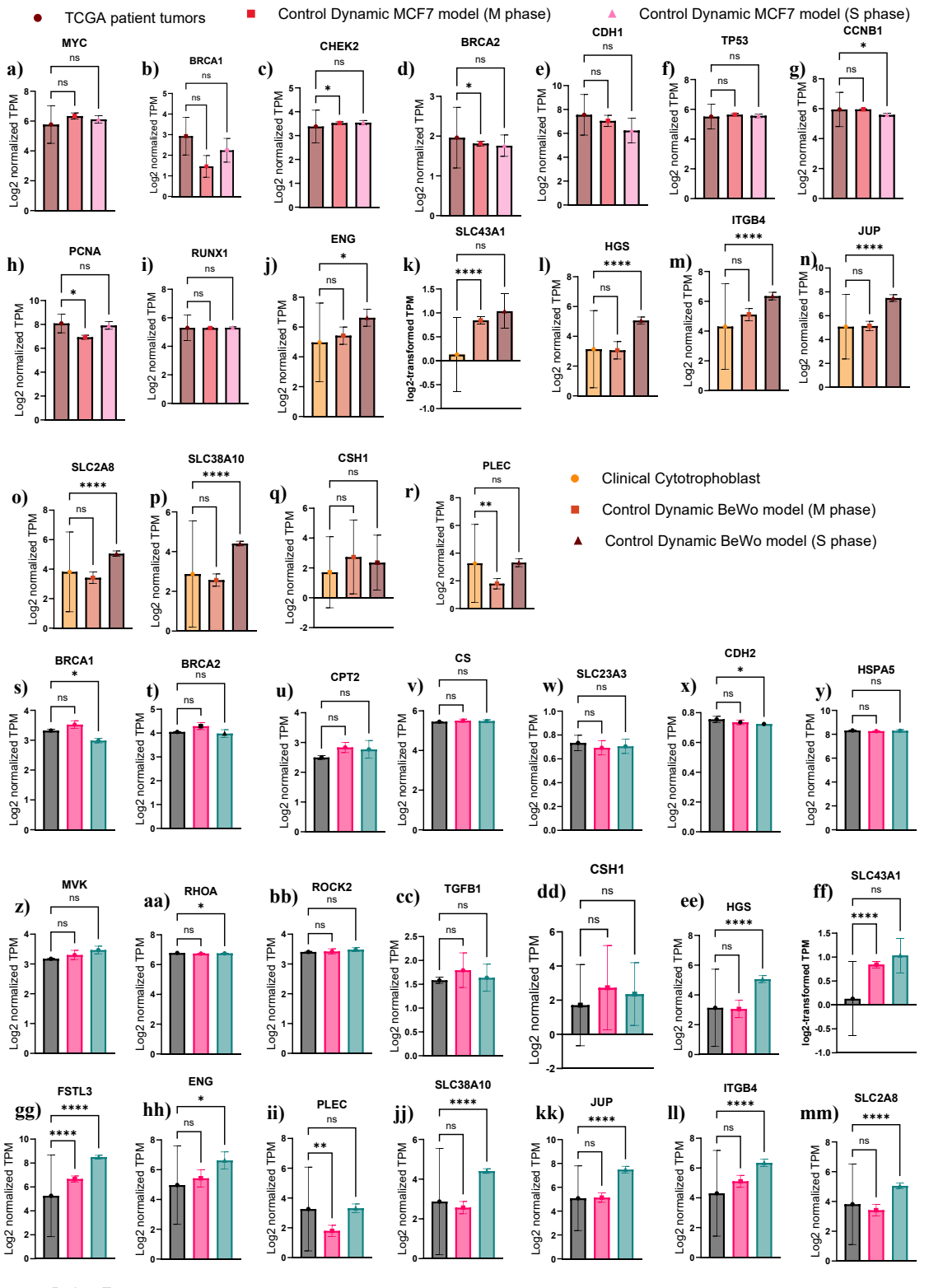

TCGA patient tumors
Control Dynamic MCF7 model (M phase)
Control Dynamic MCF7 model (S phase)
Clinical Cytotrophoblast
Control Dynamic BeWo model (M phase)
Control Dynamic BeWo model (S phase)
Patient Tumours
MCF7 of Dynamic PABC model (S-Phase)
MCF7 of Dynamic PABC model (M-Phase)
Log2 normalized TPM
log2-transformed TPM
MYC
BRCA1
CHEK2
BRCA2
CDH1
TP53
CCNB1
PCNA
RUNX1
ENG
SLC43A1
HGS
ITGB4
JUP
SLC2A8
SLC38A10
CSH1
PLEC
CPT2
CS
SLC23A3
CDH2
HSPA5
MVK
RHOA
ROCK2
TGFB1
FSTL3

Fig. 12: Clinical benchmarking validates the dynamic PABC model. (a-i) Gene-expression profiles from the control dynamic MCF7 model were compared with TCGA clinical data from patients with invasive ductal carcinoma, revealing broadly similar expression trends for key genes linked to cancer invasiveness. Bars show log_2-normalized TPM values (mean ± s.d.) for patient tumours and MCF7 control model synchronized to M-phase or S-phase .Group differences were assessed using Brown–Forsythe/Welch ANOVA with Dunnett's T3 post-hoc tests versus the patient cohort (α = 0.05).Significant differences included reduced BRCA2 (M-phase, P = 0.0404) and CCNB1 (S-phase, P = 0.0271); increased CHEK2 (M-phase, P = 0.0175); decreased PCNA (M-phase, P = 0.0118). BRCA1, CDH1, MYC, RUNX1, and TP53 showed no significant changes. Significance: *P < 0.05 = *, < 0.01 = **, < 0.001 = ***, < 0.0001 = ****; ns, not significant. **(j-r) Benchmarking of control dynamic BeWo model synchronized to M-phase or S-phase against primary clinical cytotrophoblasts**. Values are log_2-normalized TPM (mean ± s.d.). Group differences were assessed by Brown–Forsythe/Welch ANOVA with Dunnett's T3 post-hoc comparisons versus the clinical reference (α = 0.05). Expression of CSH1 did not differ significantly between groups. ENG was higher in the S-phase model (P = 0.0365), whereas SLC43A1 was significantly elevated in M- and nonsignificant in S-phase cultures (P < 0.0001). HGS, ITGB4 and JUP were markedly increased in the S-phase condition (P < 0.0001 for each). PLEC was reduced in M-phase (P = 0.0038) but unchanged in S-phase, while SLC38A10 was strongly upregulated in S-phase (P < 0.0001). **(s-mm) Expression profiles of genes in the MCF7 of the dynamic PABC model compared with pregnancy-associated breast cancer (PABC) tumors (GSE31192)**. Bars represent mean log_2(TPM) ± SD for cells synchronized in S-phase (n = 3) or M-phase (n = 3), alongside patient tumour samples (n = 6). Group comparisons were performed using Brown–Forsythe and Welch ANOVA followed by Dunnett's T3 post hoc test (familywise α = 0.05). Significant differences relative to patient tumours were observed for BRCA1 (M-phase, p = 0.010), RHOA (M-phase, p = 0.033), and CDH2 (M-phase, p = 0.025), while no significant changes were detected for BRCA2, CPT2, CS, HSPA5, MVK, ROCK2, SLC23A3, or TGFB1. These data highlight the ability of the model to recapitulate oncogenic and EMT-related transcriptional features of PABC. (p < 0.05; *p < 0.01).

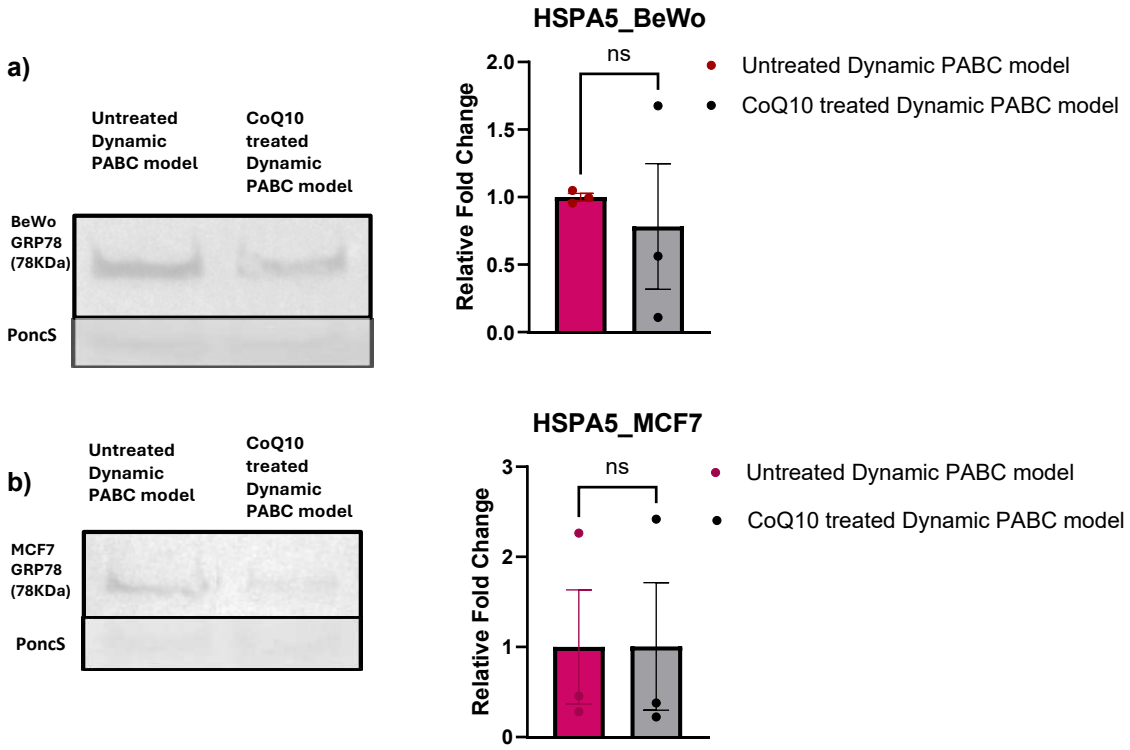


Fig. 13. Functional validation of the dynamic PABC model using CoQ10 treatment. a) Representative western blots (left panel) and quantitative analysis (right panel) showing decreased expression of GRP78/HSPA5 protein levels in BeWo cells of dynamic PABC model following CoQ10 treatment compared with the untreated control (20µg protein loaded per lane and normalized to Ponceau stain), b) In the same PABC model, MCF7 cells exhibited a similar GRP78/HSPA5 protein levels upon CoQ10 treatment compared with untreated control dynamic PABC model (20µg protein loaded per lane and normalized to Ponceau stain). Band intensities were normalized to the control dynamic PABC model (set to 1.0); bars represent mean ± s.d.

Supplementary Files

This is a list of supplementary files associated with this preprint. Click to download.

- SupplementaryFile20260217YA.docx
- SupplementaryTable20260217YA.xlsx